

LA-UR- 03-1882

Approved for public release;  
distribution is unlimited.

Title: Cosmic Ray Muon Radiography: A doctoral dissertation  
proposal

Author(s): Larry Schultz, 180899, P-25

Submitted to: Portland State University



46



Los Alamos National Laboratory, an affirmative action/equal opportunity employer, is operated by the University of California for the U.S. Department of Energy under contract W-7405-ENG-36. By acceptance of this article, the publisher recognizes that the U.S. Government retains a nonexclusive, royalty-free license to publish or reproduce the published form of this contribution, or to allow others to do so, for U.S. Government purposes. Los Alamos National Laboratory requests that the publisher identify this article as work performed under the auspices of the U.S. Department of Energy. Los Alamos National Laboratory strongly supports academic freedom and a researcher's right to publish; as an institution, however, the Laboratory does not endorse the viewpoint of a publication or guarantee its technical correctness.

# **Cosmic Ray Muon Radiography**

by  
Larry J. Schultz

A dissertation proposal submitted for consideration for partial fulfillment  
of the requirements for the degree of

Doctor of Philosophy  
in  
Electrical and Computer Engineering

Portland State University  
March 13, 2003

## Abstract

The Earth is continuously bombarded by muons generated by cosmic rays striking the atmosphere. Physicists have studied cosmic ray muons extensively, and much is known about the cosmic ray muon flux and what occurs when muons pass through objects. Relatively little practical use has been found for these cosmic ray muons, but some researchers have made use of their high penetrating ability to perform rough radiography of large geophysical objects such as mountains, and large human made structures, most notably a pyramid.

We propose to take advantage of the multiple scattering that occurs when muons move through material to perform radiography on a much smaller scale. Rather than objects the size of mountains or pyramids, we propose to radiograph objects the size of a truck, a car, a suitcase, a telephone, or smaller. Although a foundation exists for multiple scattering radiography, no attempt has ever been made to use cosmic rays muons in such a manner. In addition to demonstrating a completely new mode of radiography, we expect to develop new reconstruction techniques based on statistical signal processing and maximum likelihood methods. These topics have traditionally been investigated in electrical engineering departments.

If successfully demonstrated, this technique would find application in areas wherein radiography of relatively dense objects is needed, but application of an artificial radiographic dose is undesirable. One such application is detection of surreptitious transport of nuclear material at border crossings.

# Contents

Abstract.....	2
Contents .....	3
1. Introduction.....	4
1.1 General Proposal.....	5
1.2 Proposal Overview.....	5
2. Background.....	6
2.1 Cosmic Rays & Muons .....	6
2.1.1 Primary Cosmic Rays and the Atmospheric Cascade.....	6
2.1.2 The Muon Spectrum at the Surface .....	7
2.2 How Muons Interact with Matter.....	8
2.2.1 Energy Loss .....	9
2.2.2 Attenuation (or Range Out) .....	9
2.2.3 Multiple Coulomb Scattering.....	10
2.3 Previous Work on Cosmic Ray Muon Radiography.....	12
2.4 Previous Work on Charged Particle Radiography .....	13
2.5 Overview of Computed Tomography .....	14
2.5.1 Transform-based CT .....	15
2.5.2 Algebraic-based CT .....	18
3. Cosmic Ray Muon Multiple Scattering Radiography.....	21
3.1 Concept .....	21
3.2 Preliminary Calculations on Exposure Time .....	22
3.2.1 Material Discrimination Assuming Monoenergetic Muons .....	22
3.2.2 Material Discrimination Assuming Cosmic Ray Muon Energy Spread.....	23
3.3 Point of Closest Approach (PoCA) Reconstruction Method .....	24
3.4 Preliminary Simulated Demonstration.....	26
3.5 Momentum Measurement .....	29
4. Proposed Work.....	32
4.1 Experimental Prototype .....	32
4.1.1 System Overview.....	32
4.1.2 Time Delay Line Multi-Wire Proportional Chamber (MWPC) Detectors .....	33
4.1.3 Signal Conditioning Electronics, Data Acquisition, and Analysis. ....	35
4.1.4 Demonstration.....	35
4.2 Simulation and Validation .....	35
4.3 Reconstruction Algorithm.....	35
4.4 Application to Contraband Detection for Homeland Defense.....	36
4.5 Summary .....	37
5. Administrative Issues.....	38
5.1 Significance.....	38
5.2 Appropriateness .....	38
5.2 Timeline .....	38
5.3 Publication Targets .....	38
Appendices.....	39
Appendix 1 – Blanpied Muon Generator.....	39
References.....	44

# 1. Introduction

When cosmic rays strike the Earth's atmosphere, a cascade of many types of subatomic particles is created. By the time this shower of particles reaches the Earth's surface, it is comprised primarily of *muons*. Muons are charged particles, having about 200 times the mass of electrons (indeed, muons may be thought of as "heavy electrons," though they may be positively or negatively charged). The surface of the Earth is bombarded continuously by these muons at a rate of about 10,000 muons per minute per square meter [1]. Most cosmic ray muons have sufficient energy to penetrate meters of rock. One might think of this as "invisible rain," constantly showering down from the sky, passing unnoticed through objects and life forms into the ground, to be eventually absorbed by the Earth.

Can we make any practical use of these cosmic ray muons? They represent no substantial source of energy. They perform no usable "work" as they pass through objects. However, since muons are charged particles, they are easily detectable through means used by subatomic physicists for decades. Muons are detected by capturing and amplifying the small deposition of energy that occurs when they pass through instruments. The deposited energy is given up by the particle. Muons, then, are detectable and experience changes as they pass through material. Indeed, as will be discussed later, other interactions occur as muons pass through matter, and the degree of these changes are related to the nature of the material itself. Perhaps these changes represent an *information source* of which we might make some use.

Although we metaphorically speak of cosmic ray muons in terms of "rain," muons actually arrive not strictly from vertically overhead, but from angles covering the upper hemisphere (though preferentially from overhead, and quite sparsely from angles nearing horizontal). Since cosmic ray muons are detectable, carry information as they pass through material, and continuously bombard any position on the Earth's surface from many overhead directions, we are led to wonder: Can we use these cosmic ray muons as some sort of 3-D radiographic probe? In other words, can we use the cosmic ray muon flux to probe an object of unknown structure / material composition to enhance our knowledge about that object, as illustrated in Figure 1?

If feasible, radiography using cosmic ray muons would have some attractive features. Foremost would be that no additional radiological dose would be applied to the object. Whether or not we do the radiography, the object will be illuminated with cosmic ray muons. This is a key advantage over x-ray radiography, for instance, wherein an object receives a radiological dose that must be carefully managed to avoid undesirable effects, particularly if the object is a living being. Of course a related additional attractive feature of using cosmic ray muons is that no manufactured radiographic source is required (in a sense, we get "something for nothing"). Another potential feature of muon radiography is that, since muons are so highly penetrating, very thick, dense objects could be radiographed.

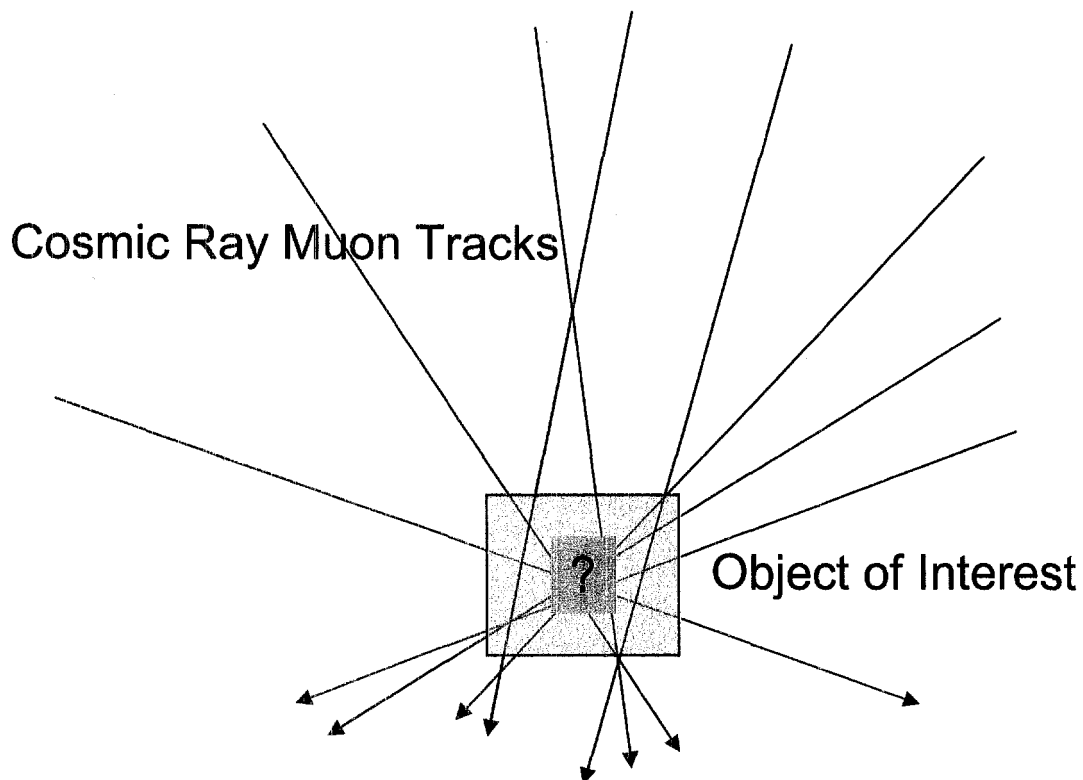


Figure 1 – Illustration of cosmic ray muons passing through an object. Measuring changes in the muons could allow for radiography of the object.

### **1.1 General Proposal**

It is proposed herein to investigate the use of cosmic ray muons for radiography of objects. The primary goal of this work will be “proof of principle.” A more detailed proposal of specific work will appear below. Generally speaking, however, we propose to build a small experimental prototype, develop object reconstruction algorithms, and demonstrate through example the feasibility of cosmic ray muon radiography. We will also develop and validate a simulation and use that simulation to investigate larger, more complex scenarios and applications than can be reasonably investigated experimentally.

### **1.2 Proposal Overview**

In Chapter 2 we present background information on several pertinent topics. We discuss cosmic ray muons; how they are formed, and what is known about the muon flux at the Earth’s surface. The physics of interaction of muons with material is summarized. We review some relevant prior radiographic work. We also discuss some pertinent background on techniques for computed tomography. Details of our specific concept for cosmic ray muon radiography appear in Chapter 3. We outline the basic idea, and illustrate it with some simple analytical examples and simulations. In Chapter 4 we outline the specifics of the proposed work, and introduce one potential application – contraband detection for homeland defense. In Chapter 5 we address some administrative issues related to the nature of the proposed work towards an electrical engineering dissertation.

## 2. Background

In this section we discuss some background information pertinent to the investigation of using cosmic ray muons for radiography. We will introduce the muon particle, discuss how cosmic rays create muons in the atmosphere, describe the flux of cosmic ray muons at the Earth's surface, and explain how muons interact when passing through material. We will also review some previous efforts to use cosmic ray muons as information probes, and discuss some relevant research into radiography using other charged particles. Finally, we will briefly discuss computed tomography.

### 2.1 Cosmic Rays & Muons

#### 2.1.1 Primary Cosmic Rays and the Atmospheric Cascade

Although cosmic radiation is often thought to come from the sun, in truth cosmic radiation comes generally from outside the solar system [1]. Cosmic rays striking the Earth's atmosphere are hence composed primarily of stable particles and nuclei which survive the trip. When these "primary" cosmic rays strike the Earth's atmosphere, interactions take place which generate additional "secondary" particles. Interactions of these secondary particles create more particles, and a cascade of particles is created.

It is beyond our scope to dwell on the details of the nuclear physics involved in creating the secondary cosmic ray flux at the Earth's surface. However, the basics may be described in simple terms. An individual *proton* or nuclei strikes the atmosphere and collisions with atmospheric nuclei release secondary particles known as *pions*. The primary proton loses energy via these collisions, but while it survives many pions may be produced. Pions may be positively or negatively charged or may be neutral. Charged pions decay quickly to like charged *muons* and neutral *neutrinos*. Neutral pions decay to gamma rays, some of which produce electron-positron pairs which generally do not survive to reach the surface. Muons lose energy as they pass through the atmosphere, but most cosmic ray muons are sufficiently energetic to reach the surface. Figure 2a illustrates this cascade. Because muons have a relatively longer lifetime than other charged particles generated in the cascade, they dominate the surface spectrum, as illustrated in Figure 2b. Muons have a rest mass of 105.7 Mev [1], about 200 times that of electrons, and are sometimes referred to as "heavy electrons." They have a mean life of 2.2  $\mu$ s [1], and may be positively or negatively charged.

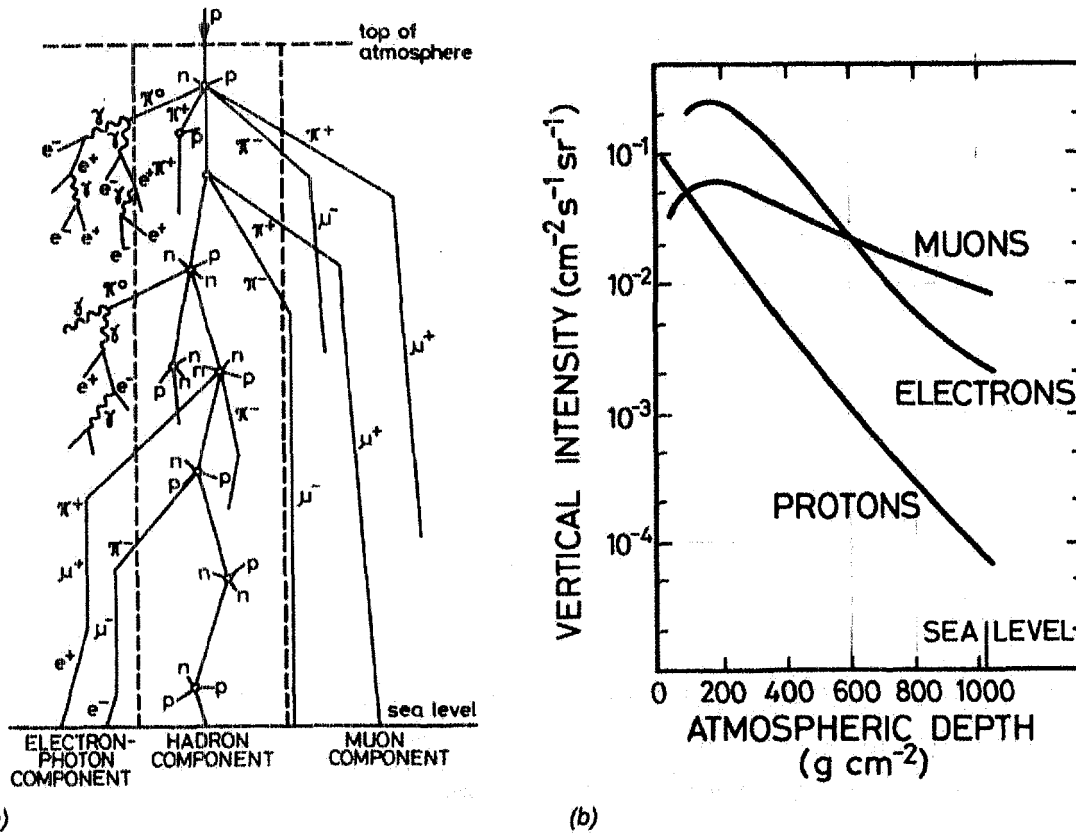


Figure 2 – Illustration of the particle cascade produced in the atmosphere from a primary cosmic proton (a). Altitude variation of the main components in the cascade (b) (From [2], used with permission).

### 2.1.2 The Muon Spectrum at the Surface

Muons arrive at a point on the Earth's surface from angles spanning the upper hemisphere and with a wide range of energies. The angle and energy distribution reflects a convolution of the production spectrum, energy loss in the atmosphere, and decay. The surface spectrum varies with altitude, geophysical location, and the level of solar activity (since solar activity can modulate the primary cosmic ray spectrum). Many researchers have experimentally documented the muon spectrum at various locations and altitudes and have modeled the production process ([3, 4, 5, 6, 7], for example).

Illustrative data taken from two experiments is shown in Figure 3, for arrival angles of near  $0^\circ$  and  $75^\circ$ . Analytical models such as that presented in [3], coupled with such experimental data, have been used to develop "muon generators" for simulation purposes. Results from a model developed by Blanpied [8] are shown in Figure 3.



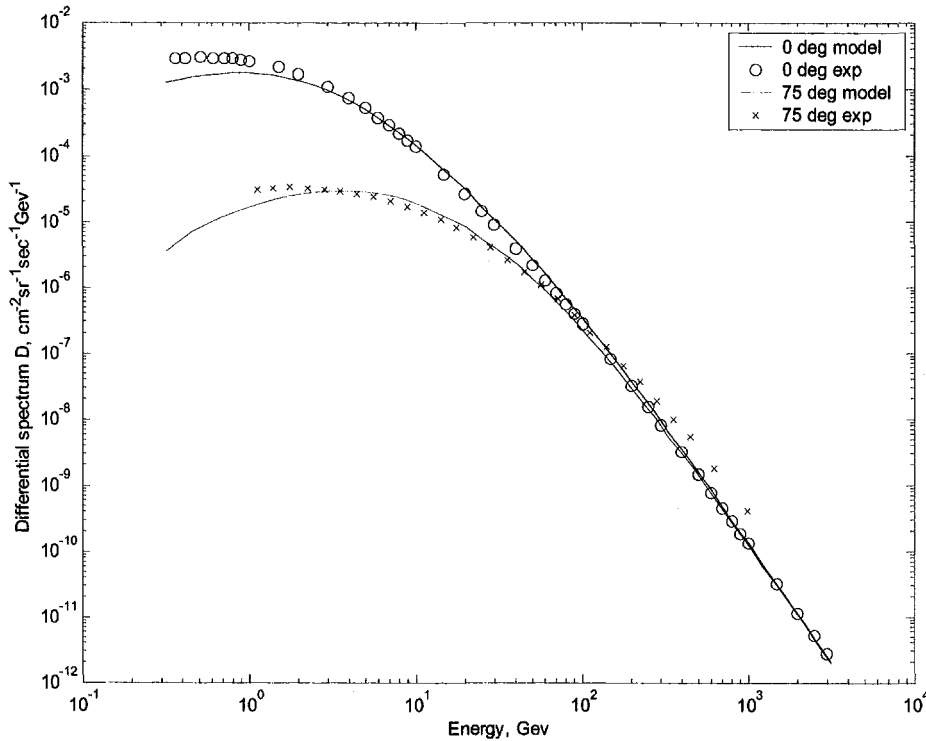


**Figure 3 – Experimental muon spectrum data for two arrival angles; 0° data taken from [5], 75 ° data from [4]. The model lines were generated from a model developed by Blanpied [8].**

Experimentalists often refer to the following “rules of thumb” to describe the muon spectrum [1]:

- The energy distribution is almost flat for energies below 1 GeV, and transitions to follow  $p^{-2.7}$  for energies above 10 GeV. The mean muon energy is about 4 GeV.
- The angular distribution goes approximately as  $\cos^2(\theta)$ , where  $\theta$  is angle from vertical.
- The overall muon rate is approximately  $10,000 \text{ m}^{-2} \cdot \text{min}^{-1}$  for horizontal detectors.

It is important to note that the muon rate is low enough (about 160 Hz in a square meter detector) to enable single event processing, but perhaps high enough to provide information in a reasonable amount of time in a radiographic scenario.

## **2.2 How Muons Interact with Matter**

Muons in the .1-1000 GeV energy range interact with matter in two primary ways, energy loss through electromagnetic interaction with electrons resulting in ionization, and deflection via multiple Coulomb scattering from interactions with nuclei, as illustrated in Figure 4. Sufficient energy loss will cause a muon to stop, which is highlighted as a third “interaction”.

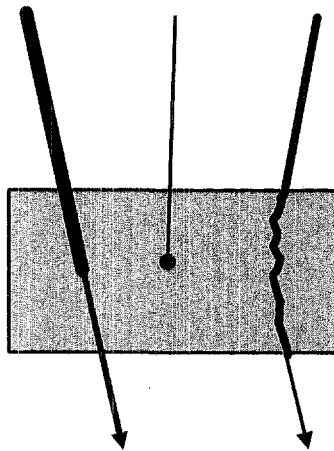


**Figure 4 – Muon interactions when passing through matter.** Muons lose energy through ionization (blue). If enough energy is lost, muons will stop (red). Muons are also deflected via multiple Coulomb scattering (green). These interactions are shown separately for clarity, although all three are applicable to any particle.

### 2.2.1 Energy Loss

As muons pass through material and collide with electrons, these electrons are (predominantly) ejected from the atom. The muon will lose energy equivalent to the ionization energy of the electrons with which it collides. For muons in the .1-1000 Gev energy range, about 2.2 Mev of energy is lost per  $\text{g}\cdot\text{cm}^{-2}$  of material traversed [1]. The energy loss of muons traversing 10 cm thicknesses of various materials is shown in Table 1.

Table 1. Approximate energy loss experienced by muons traversing 10 cm of various materials.

Material	Volume Density, $\text{g}\cdot\text{cm}^{-3}$ [1]	Areal Density of 10 cm depth, $\text{g}\cdot\text{cm}^{-2}$	Muon Energy Loss, Mev	% Energy Loss for 4 Gev Muon
Water	1.00	10.0	22.0	0.6%
Concrete	2.50	25.0	55.0	1.4%
Iron	7.87	78.7	173.1	4.3%
Lead	11.35	113.5	249.7	6.2%
Uranium	18.95	189.5	416.9	10.4%

Energy loss is a potential information source that could be tapped for radiography, since energy loss is proportional to the mass encountered by a particle traversing an object area. A means for the relatively precise measurement of energy of incoming and outgoing particles would be required.

### 2.2.2 Attenuation (or Range Out)

If enough energy is lost through ionization, a muon will stop (range out) within the material. Precise calculation of the range of particles within materials involves integration of the energy loss relationship outside the energy range where the 2.2 Mev loss per  $\text{g}\cdot\text{cm}^{-2}$  is appropriate. However, we may approximate the range as the material

depth at which all energy is lost, using the  $2.2 \text{ Mev}\cdot\text{cm}^2\cdot\text{g}^{-1}$  figure. Results are shown in Table 2 for the same materials as in Table 1, for various muon energies.

Table 2. Approximate range of muons in various materials.

Material	Volume Density, $\text{g}\cdot\text{cm}^{-3}$ [1]	Range (m) of Muons with Energy		
		0.4 Gev	4 Gev	40 Gev
Water	1.00	1.8	18.2	181.8
Concrete	2.50	0.7	7.3	72.7
Iron	7.87	0.2	2.3	23.1
Lead	11.35	0.2	1.6	16.0
Uranium	18.95	0.1	1.0	9.6

Interesting to note is that muons at the mean energy will penetrate over a meter of even very dense materials, and high energy muons will penetrate tens of meters of rock or metal. Attenuation might be an attractive information source to use in the radiography of very large, dense objects. Indeed previous researchers have attempted attenuation radiography of large objects using cosmic ray muons (see section 2.3).

On the other hand, the attenuation of low energy muons might serve as an information source that could be used to highlight moderate sized (say 10 cm cubes) of metal within lower density surroundings. This information source would be relatively sparse, since muons with energy below 1 Gev constitute only about 10-15% of the spectrum (estimated using Blanpied model [8]).

### 2.2.3 Multiple Coulomb Scattering

A muon (or any charged particle) passing through a material is deflected by many small angle scatters off of the nuclei of the material. As illustrated two dimensionally in Figure 5, the particle will traverse the material in a stochastic path due to these multiple scatters. The particle will emerge from the material at an aggregate scattered angle  $\theta$  and displaced from the un-scattered exit point by a distance  $x$ . Multiple scattering has been extensively modeled and studied experimentally (see [1,9,10], for example). The angular scattering distribution is approximately Gaussian, with zero mean and a standard deviation given by [1]:

$$\sigma_{\theta} = \frac{13.6 \text{ Mev}}{\beta c p} z \sqrt{\frac{L}{L_0} \left[ 1 + 0.038 \ln \left( \frac{L}{L_0} \right) \right]} \quad (1)$$

where  $p$ ,  $\beta c$ , and  $z$  are the momentum, velocity and charge number of the incident particle,  $L$  is the depth of the material, and  $L_0$  is the radiation length of the material. For muons,  $\beta c=1$  and  $z=\pm 1$  depending on the muon charge, but sign is irrelevant. Radiation length is a characteristic amount of matter for scattering and other nuclear interactions, and decreases with increasing material  $Z$  number.

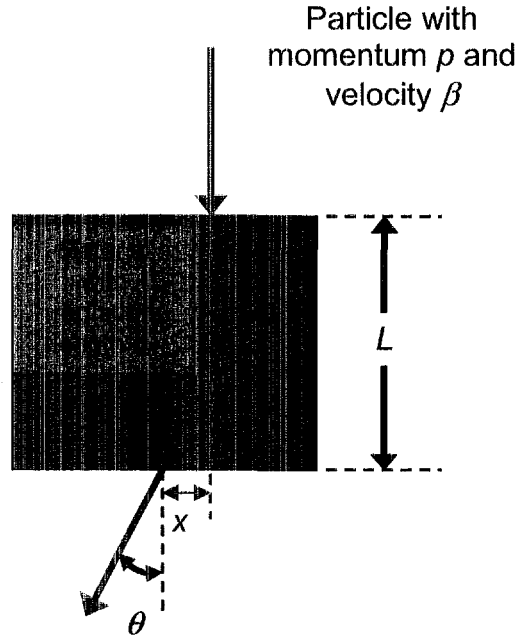


**Figure 5 – Multiple Coulomb scattering of a charged particle through material. The magnitude of scattering is exaggerated for illustrative purposes.**

In Table 3 we show how the width of the scattering distribution changes for muons passing through 10 cm of the Table 1 materials:

**Table 3. Approximate multiple scattering for muons passing through 10 cm of various materials**

Material	Radiation Length, cm [1]	RMS Scattering (milliradians) expected for Muons with Energy:		
		0.4 Gev	4 Gev	40 Gev
Water	36.1	17.0	1.7	0.2
Concrete	10.7	32.8	3.3	0.3
Iron	1.76	86.4	8.6	0.9
Lead	0.56	159.4	15.9	1.6
Uranium	0.32	214.9	21.5	2.1

Multiple scattering represents an information source that is almost as sensitive to material difference as energy loss. Moreover, the measurement of muon scattering with milliradians precision (by measuring particle position to millimeter level precision) is much more easily accomplished than measurement of particle energy to a few percent (requiring the generation of magnetic fields for spectroscopy). It is the multiple scattering signal that we propose to use for our information source, as will be detailed in section 3.

### **2.3 Previous Work on Cosmic Ray Muon Radiography**

Several researchers have investigated the use of cosmic ray attenuation or range radiography for large archaeological or geological objects. The most famous of these is Luis Alvarez's radiography of the Pyramid of Chepren at Giza, Egypt in the late 1960's [11]. The Pyramids of Cheops (Chepren's father) and Sneferu (his grandfather) were known to contain interior chambers at similar locations. It had been speculated that Chepren's Pyramid might also contain similar interior chambers, but they had not been discovered. Alvarez and his colleagues sought to locate (or disprove the existence of) these chambers by measuring the attenuation of cosmic rays through the Chepren's Pyramid. Alvarez and his colleagues placed muon counters in an existing underground chamber beneath the pyramids. As they rotated their counters about the 360 azimuth, they experienced higher count rates when pointing at the faces of the pyramid than when pointing at the corners since the path length of cosmic rays passing through the corners was longer. The position of their underground chamber was not centered beneath the pyramid, and they were also able to see count rate differences when pointing at opposite faces that were proportional to that deviation from center position. Armed with this confirmation of their method, they searched for hidden chambers and concluded that there were none.

In subsequent years other researchers have followed Alvarez and used cosmic ray attenuation to make measurements on large objects. Minato [12] produced a rough radiograph of the Higashi-Honganji Temple gate in Nagoya, Japan, using a simple hand held muon counter to measure flux attenuation. Nagamine [13] measured the internal structure of Mt. Tsukaba and Mt. Asama using cosmic ray attenuation with the goal of volcanic eruption prediction. In this case large angle (nearly horizontal) muons were required, since detectors were located 2 km to the side of the volcanoes, rather than beneath them, of course.

These interesting experiments and others like them, rely on attenuation of high energy cosmic ray muons passing through meters of dense material. What we are proposing is fundamentally different, as will be seen in Section 3, and we expect to radiograph much smaller, less dense objects.

A recent novel use of cosmic ray muons has been described by Frlez, et. al [14]. Their objective was to map the efficiency of cesium iodide crystals used for calorimetry. Cosmic ray muons were used as a freely available probe to measure the efficiency of the crystals. Muon detectors were arranged above and below a chamber containing several of the CsI crystals, and rays were tracked through the chambers / crystals. For cosmic rays passing through a crystal, the path length and resultant expected energy deposition were calculated. Hence, the response of the CsI crystals to that energy deposition could be analyzed. Here cosmic ray muons were used for a much different purpose than we propose, but the detection and data acquisition system used is very similar to what we will propose herein.

In summary, cosmic ray muons have been used in the past as radiographic probes, but, to our knowledge, no attempt has been made to use the multiple scattering of cosmic ray muons through material as an information source.

## 2.4 Previous Work on Charged Particle Radiography

Multiple scattering of charged particles as a radiographic information source has been proven through *proton radiography* (pRAD) [15]. pRAD was invented at Los Alamos National Laboratory in 1995 and is currently used routinely for radiography of moderately dense objects that are difficult to image with x-rays. pRAD is performed using an 800 Mev proton beam from a linear accelerator. A schematic is shown in Figure 6.

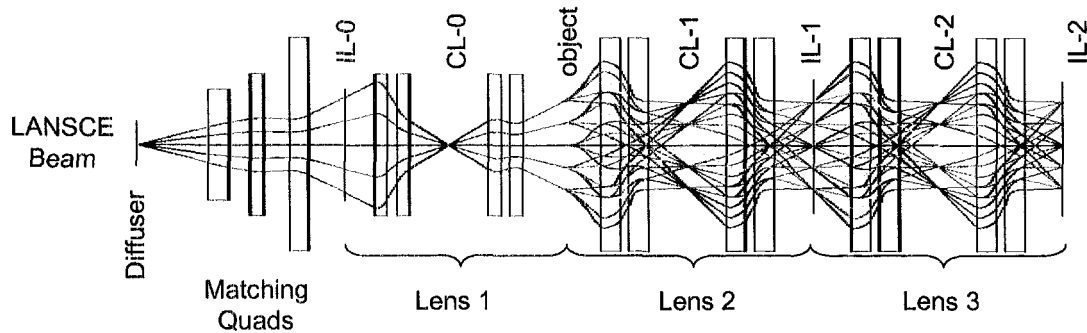
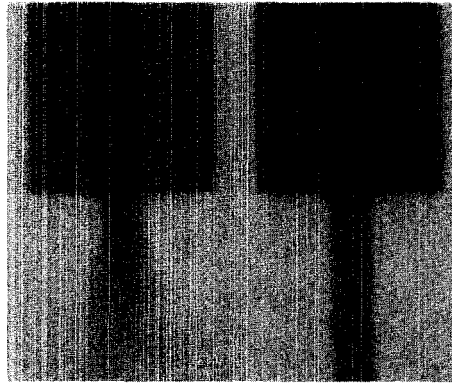


Figure 6 – Schematic of proton radiography beam line.

Simply put, pRAD works by illuminating an object (labeled object in Figure 6) with a proton beam, producing multiple scattering. The angular distribution of proton beam exiting the object is then locally (spatially) correlated with the projected density of the material through which the beam passed. Different degrees of scattering are shown in different colors in Figure 6. A clever arrangement of magnetic lenses transforms particle angle to radial position at the collimator (CL-1) location. At the collimator location, particles with large scattering angle are attenuated. For example, the black and blue rays might be removed. Another magnetic lens re-transforms the particles back to the spatial coordinates at the image plane (IL-1). So at the image plane, areas where the object induced high scattering are less populated with protons due to the collimation. A proton to light converter and CCD cameras produce an image. In Figure 6 an additional collimator (CL-2) and imaging station (IL-2) are shown. A example pRAD image is shown in Figure 7.



**Figure 7 – Example images created via multiple scattering radiography (pRAD). The darker areas represent higher Z material.**

The pRAD method is pertinent to our proposal for cosmic ray muon radiography in that it provides proof of the feasibility of multiple scattering as a radiographic information source. However, pRAD imaging is based on large number statistics, whereas we will propose to work with single events. Also, we will obviously not be requiring a linear accelerator.

Charpak, et al. [31] investigated using *nuclear (hadronic) scattering* of protons passing through material as an information source for radiography. They used protons generated by an accelerator, and detected particles scattered via hadronic interactions. By tracing incoming and outgoing trajectories to an intersection point, they identified the point of scatter within an object volume, and used the information gathered from many scattered particles to reconstruct object density. We propose to investigate a similar algorithm for cosmic ray muon radiography, as will be discussed in Sections 3.1 and 3.3.

## **2.5 Overview of Computed Tomography**

Tomography refers to the reconstruction of an image or object from projections taken from many different directions. Tomographic reconstruction and the associated signal processing represent an area of active research, primarily in the electrical engineering and mathematical fields. The mathematics of this reconstruction process were analyzed early in the 20<sup>th</sup> century by Radon, as outlined in the historical review in [16]. Widespread interest in tomographic imaging was spawned much later after the invention of the computed tomography (CT) x-ray scanner by Hounsfield [17], for which he received a Nobel Prize. Since then the techniques for CT have been continuously evolved, taking advantage of the rapid advances in computing power over the last three decades. A variety of information sources have been used for CT, including x-ray attenuation, reflection of radar pulses, gamma ray emission, ultrasound, and magnetic resonance. Tomographic techniques have been used to reconstruct 3-dimensional objects from 2-dimensional proton radiography (see section 2.4) projections.

It is beyond our scope to cover the array of CT techniques and applications, many of which are highly specialized. There are, however, two major families of techniques for reconstruction from projections: transforms methods and algebraic methods. We will touch briefly on each of these.

### 2.5.1 Transform-based CT

Transform based methods are used in the bulk of CT applications. Unfortunately, it will be seen that transform methods are inappropriate for the research proposed herein. However the frequency domain interpretation of projection data allows for intuitive understanding of the reconstruction process and difficulties that can occur when data is limited. Since we expect to be dealing with sparse data, it is instructive to outline the basics of transform based CT (summarized from a presentation in [16]).

Referring to Figure 8a, we may mathematically express a projection through line integrals. If  $f(x,y)$  represents some measurable function, characteristic of the object, which varies spatially (x-ray attenuation coefficient, for example), and we pass a parallel beam of rays through the object, oriented at angle  $\theta$ , we create a projection  $P_\theta(t)$ , where the dimension  $t$  may be described via the equation:

$$t = x \cos \theta + y \sin \theta \quad (2)$$

We may express the projection by the integration (known as the *Radon Transform*):

$$P_\theta(t) = \int_{-\infty}^{\infty} \int_{-\infty}^{\infty} f(x,y) \delta(x \cos \theta + y \sin \theta - t) dx dy \quad (3)$$

We create a number of projections by rotating through various angles, as shown in Figure 8b, and seek to reconstruct  $f(x,y)$  from those projections.

It is in the frequency domain that the nature of sampling the image via projections becomes clear. Let us first define the 2-dimensional Fourier transform of the object function:

$$F(u,v) = \int_{-\infty}^{\infty} \int_{-\infty}^{\infty} f(x,y) e^{-j2\pi(ux+vy)} dx dy \quad (4)$$

and the one dimensional Fourier transform of a projection is:

$$S_\theta(w) = \int_{-\infty}^{\infty} P_\theta(t) e^{-j2\pi wt} dt \quad (5)$$

The Fourier Slice Theorem allows us to interpret projections in the frequency domain. To illustrate the theorem, let us consider the Fourier transform of the object along a line in the frequency domain where  $v = 0$ :

$$F(u,0) = \int_{-\infty}^{\infty} \int_{-\infty}^{\infty} f(x,y) e^{-j2\pi ux} dx dy = \int_{-\infty}^{\infty} \left[ \int_{-\infty}^{\infty} f(x,y) dy \right] e^{-j2\pi ux} dx \quad (6)$$

Let us also write the equation for the projection when  $\theta = 0$ :

$$P_{\theta=0}(t) = \int_{-\infty}^{\infty} \int_{-\infty}^{\infty} f(x,y) \delta(x-t) dx dy = \int_{-\infty}^{\infty} f(x,y) dy \quad (7)$$

We note that the term in brackets in Eq. (6) is just the projection defined in Eq. (7). Substituting:

$$F(u,0) = \int_{-\infty}^{\infty} P_{\theta=0}(x) e^{-j2\pi ux} dx \quad (8)$$

Eq. (8) may be recognized as the one-dimensional Fourier transform of the projection  $P_{\theta=0}$ , therefore:

$$F(u,0) = S_{\theta=0}(u) \quad (9)$$



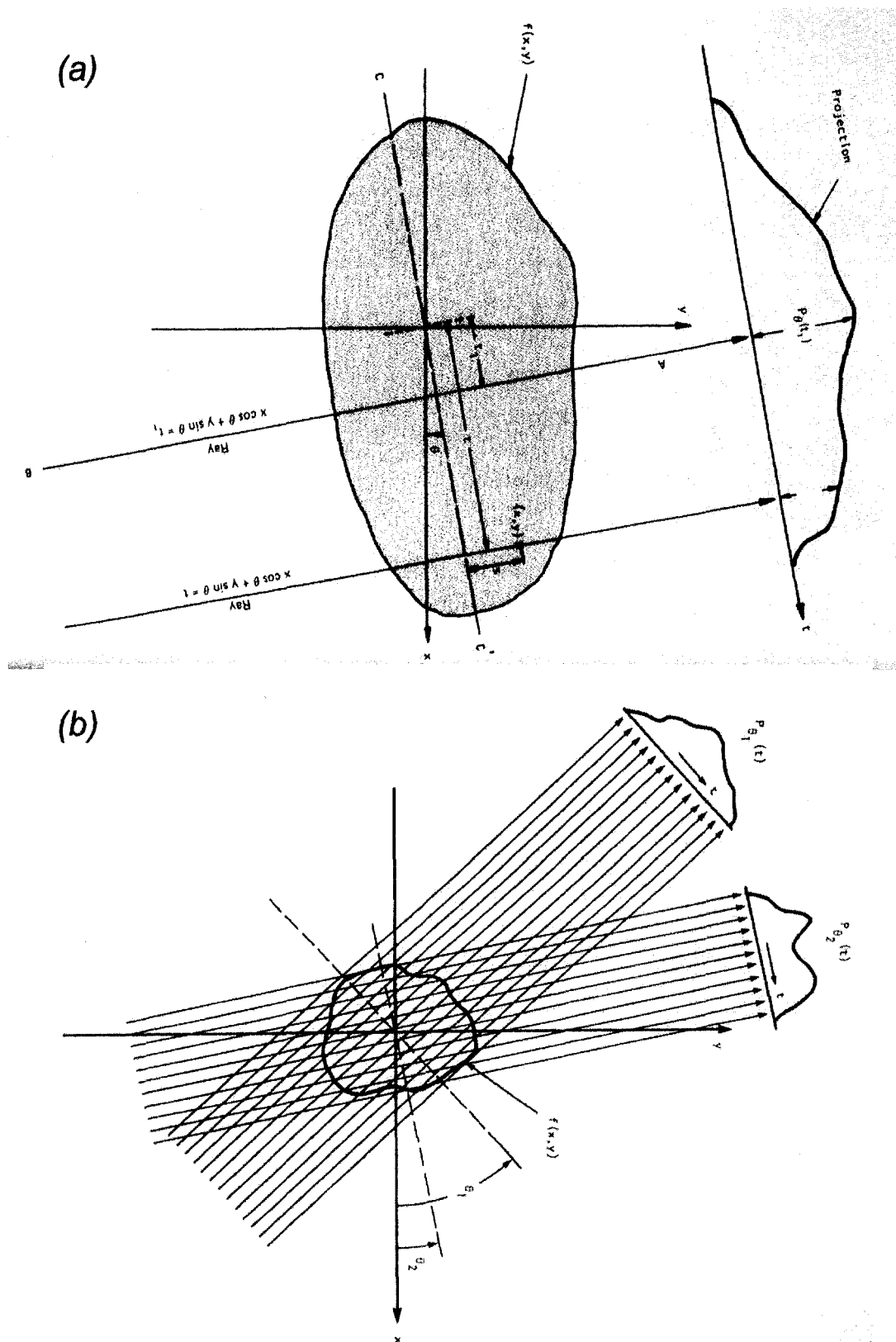


Figure 8 – Illustration of projections in CT. An object and its projection at angle  $\theta$  (b), and multiple projections at different angles (from [16], used with permission).

This result is independent of the specific angle  $\theta$ , and leads to the Fourier Slice Theorem, which is illustrated in Figure 9a and b, and may be stated as:

The Fourier transform of a parallel projection of an image  $f(x,y)$  taken at angle  $\theta$  gives a slice of the two-dimensional transform,  $F(u,v)$ , subtending an angle  $\theta$  with the  $u$ -axis. In other words, the Fourier transform of  $P_\theta(t)$  gives the values of  $F(u,v)$  along the line BB in Figure 9b.

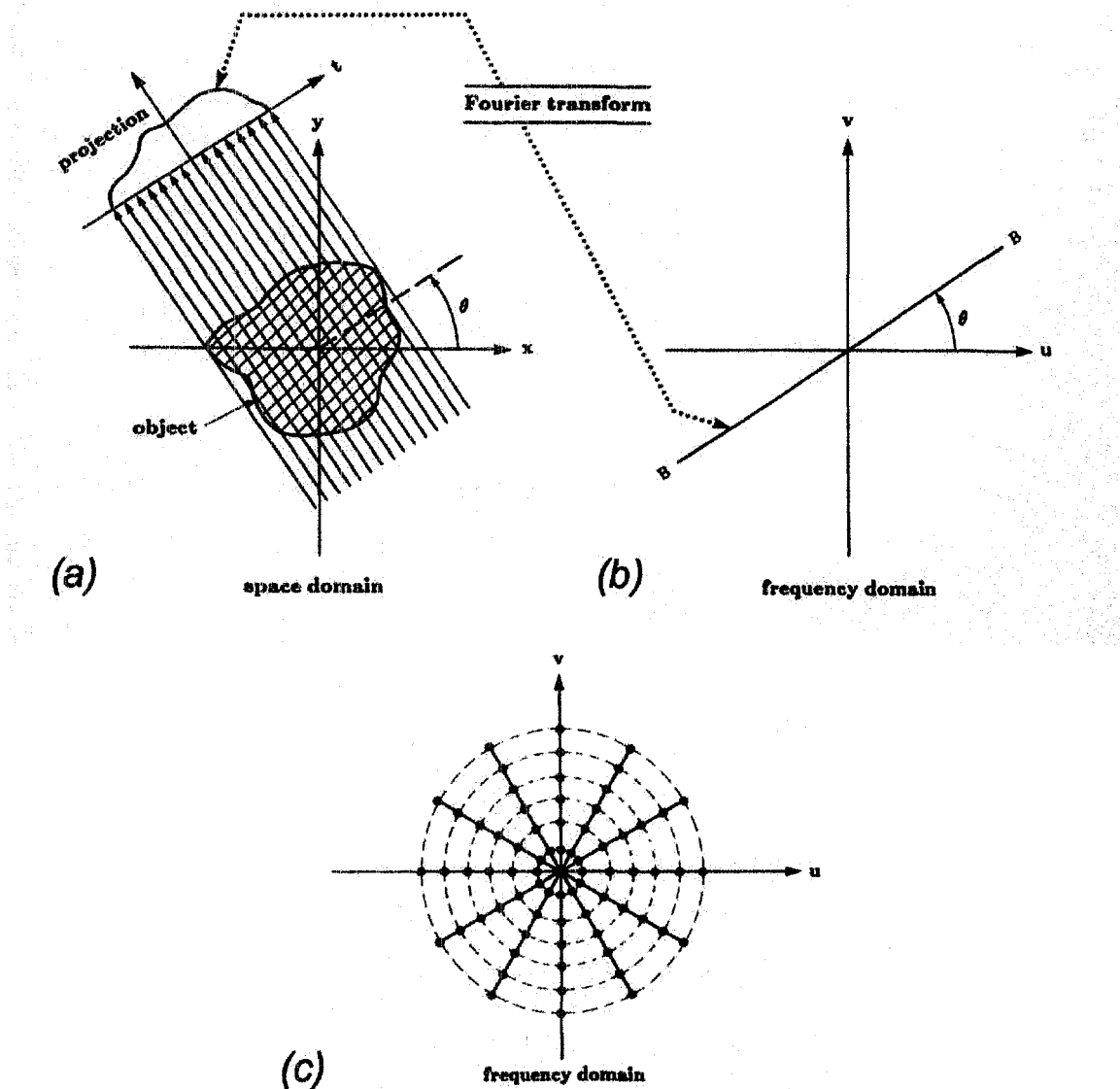


Figure 9 – Illustration of how projections may be interpreted in the frequency domain. A projection of an object at angle  $\theta$  in the space domain (a), when Fourier transformed, gives a slice of the two-dimensional transform of the object at an angle  $\theta$  (b). The FFT of multiple projections represents samples of the object FFT as shown in (c) (from [16], used with permission).

Therefore, we may interpret multiple projections at different angles as providing sampling of the frequency domain representation of the object, as illustrated in Figure 9c, where the dots show sampled points obtained when using an FFT and finite data.

One may note from Figure 9b that density of the sampled points becomes sparser as one moves farther from the center. If we are to reconstruct the object from projections, this implies that there will be more error in reconstructing the high frequency content of the image than in the low frequency content. Further imagine that we had no projections from angles near horizontal ( $\theta$  nearing  $\pm 90^\circ$ ). In this case we would expect significant error in the vertical details of the reconstruction. If we have projections from evenly spaced angles, but only a very few projections, we expect a general degradation of the fine detail of the reconstruction. Insufficient number of samples in each projection, or an insufficient number of projections can also lead to artifacts from aliasing due to under sampling.

We conclude this discussion with an outline of reconstruction based on this theory. The basic transform based reconstruction algorithm used in most straight ray tomographic applications is known as *filtered backprojection*. Making use of the Fourier Slice Theorem, the basic steps are:

1. Measure the projections.
2. Transform the projections.
3. Apply a filter to the transforms of the projections to properly interpolate them in the frequency domain.
4. Compute the inverse transform of the filtered projections.
5. Sum over the image plane all the inverse transformed filtered projections to obtain the reconstruction.

### 2.5.2 Algebraic-based CT

The filtered backprojection algorithm presented in the previous section is simple, efficient, and works well under certain conditions. However, projections evenly spaced over at least  $180^\circ$  are generally required. Ray paths must be predominantly straight – significant bending due to refraction, for example, will cause problems. In some cases (as in the research proposed herein, as will be seen) there is no notion of a projection at all. For such applications, *algebraic based CT* may provide acceptable reconstructions.

Algebraic methods consist of expressing the unknown object in terms of a finite set of parameters, and posing the reconstruction problem as a set of algebraic equations in terms of those parameters and the measured “projection” data. Then a solution for the parameters is sought. We will summarize the basics of Algebraic Reconstruction Techniques (ART), again following Kak and Slaney [16].

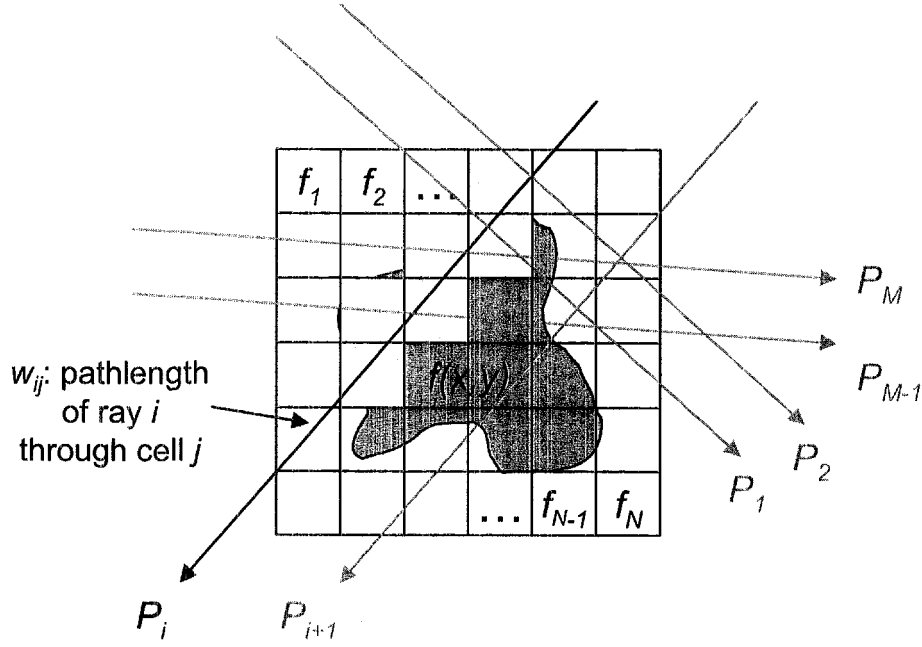


**Figure 10 – In Algebraic Reconstruction Techniques (ART), the object is broken into a discrete grid, and ray projections are modeled as weighted sums of cell values.**

We begin by superimposing a square grid over the object, as shown in Figure 10 for a two dimensional case. We will assume that the function  $f(x,y)$  is constant within each cell, and denote these discrete estimates as  $f_1, f_2, \dots, f_N$ . In Figure 10, we show a few rays passing through the object at different angles – let us assume that there are a total of  $M$  rays in our dataset. Here, we will use the term projection to refer to the line integral of a single ray in terms of the discrete version of the object. For a given ray, we may express the projection as:

$$P_i = \sum_{j=1}^N w_{ij} f_j \quad (10)$$

where the weight  $w_{ij}$  represents the normalized path length of the ray  $i$  through cell  $j$ . For simplicity we are assuming the rays are lines – if the rays had some finite width then the weights would become fractions of the cell areas. We may express the aggregate dataset through the matrix equation:

$$P = Wf \quad (11)$$

Although Eq. (11) appears to be an ordinary set of linear equations and one is tempted to simply invert the matrix  $W$  and solve for  $f$ , this is typically not possible, since:

1. The size of  $W$  can be enormous. If the object grid is  $256 \times 256$ , for example, and we have at least one ray per element, then the size of  $W$  is about  $65,000 \times 65,000$ . For three dimensional reconstruction,  $W$  is huge even for small sized problems.
2. The system is often underdetermined, i.e.,  $M < N$ .
3.  $W$  may not be invertible, even if  $M = N$ .
4. The matrix  $W$ , the vector  $P$ , and the function  $f(x,y)$  are typically nonnegative, so we desire a solution for  $f$  that is nonnegative.

Nevertheless, iterative numerical techniques may be applied to search for a solution to Eq. (11). In ART algorithms, we start with a initial guess for  $f$ , call it  $f^{(0)}$ . We will iteratively adjust that estimate via some means; after iteration  $k$  we will term the guess  $f^{(k)}$ . Let us consider a particular measured projection  $P_i$ , and define  $Q_i$  in terms of our guess  $f^{(k)}$  as:

$$Q_i^{(k)} = W_i f^{(k)} \quad (12)$$

where  $W_i$  is the  $i^{th}$  row of the weight matrix  $W$ . To enforce consistency between  $P$  and  $Q$ , we might make an adjustment to obtain  $f^{(k+1)}$  as follows:

$$f^{(k+1)} = f^{(k)} + \frac{P_i - Q_i^{(k)}}{W_i^T W_i} W_i^T \quad (13)$$

In other words, we take the difference between the measured projection for a ray and the projection that would result from our estimate, normalize that difference using the norm of that ray's weight vector, then weight the correction across elements of  $f$  by that ray's weight vector.

The update equation in the original form of ART [18] was simplified from Eq. (13) by replacing the element in the weight matrix by 0's and 1's, depending on whether the centers of image cells were within each finite width ray. A positivity constraint was also imposed, resulting in:

$$f^{(k+1)} = \max \left( 0, f^{(k)} + \frac{P_i - Q_i^{(k)}}{N_i} \right) \quad (14)$$

where  $N_i$  is the number image cells with non-zero weights for the  $i^{th}$  ray, and the correction is applied only to those image cells.

A plethora of refinements and application specific revisions have been made to ART over the years. One particular variation [18], sometimes called "ART with a Damping Factor," addresses the non-convergence of ART when noise is present in the projection data by introducing a "damping factor:"

$$f^{(k+1)} = \max \left( 0, f^{(k)} + \Delta \frac{P_i - Q_i^{(k)}}{N_i} \right) \quad (15)$$

where the damping factor,  $0 < \Delta < 1$ , can be adjusted to achieve convergence. This version of ART may be seen as equivalent to the LMS algorithm for tuning adaptive filters developed by Widrow [19], and more generally known as *stochastic gradient descent* [20]. We may therefore view Algebraic Reconstruction Techniques as a special form of gradient descent optimization.

In summary, algebraic reconstruction techniques provide a framework for creating tomographic reconstructions when data do not conform to the requirements of transform based techniques. We have shown that ART is closely related to gradient descent optimization, and so exists within a much larger general framework. It will be seen that the application proposed herein will not meet the requirements of transform based techniques, so algebraic methods are likely to be useful.

### 3. Cosmic Ray Muon Multiple Scattering Radiography

In this section we will describe our new concept for cosmic ray muon radiography. We provide a general description of our basic concept, and then apply some simple analytical and simulation techniques to illustrate the ability of our proposed technique to discriminate between materials of different atomic densities with modest exposure times. We then present newly developed object reconstruction technique and demonstrate it through simulation. Finally, we discuss the issue of energy spread in the cosmic ray muon spectrum, and how we might roughly measure individual particle momentum and apply that knowledge to improve material discrimination rate and reconstruction quality.

#### 3.1 Concept

In section 2.1 we described the cosmic ray cascade that results in a sea level muon flux of approximately  $10,000 \text{ m}^{-2} \cdot \text{min}^{-1}$ . In section 2.2 we discussed how muons interact with matter, including multiple scattering that represents an information source pertaining to the material through which the muons pass. In section 2.4 we referenced proton radiography, a demonstration of the feasibility of using multiple scattering of charged particles for radiography. In section 2.5 we reviewed how object structure may be reconstructed from measured projection data through tomographic methods. We propose to build on this body of information to radiograph and reconstruct objects via the information carried by the multiple scattering of cosmic ray muons.

Our concept is illustrated in Figure 11. Muon detectors are located above and below a target volume wherein objects of interest are located. Individual muons are tracked into and out of the object volume. This is possible due to the low event rate. Two position sensitive detectors are located above the object volume, and two below. Each detector measures particle position in two orthogonal coordinates. Via the pair of detectors above the object volume, separated vertically, the angle of the incoming track may be calculated. Muons pass through the object volume, and those that pass through dense objects are scattered more than those that pass through less dense objects. Rays that do not pass through objects are not scattered (except through the detectors, which should be designed to scatter the particles very little). Scattered muon tracks are measured by the bottom pair of detectors.

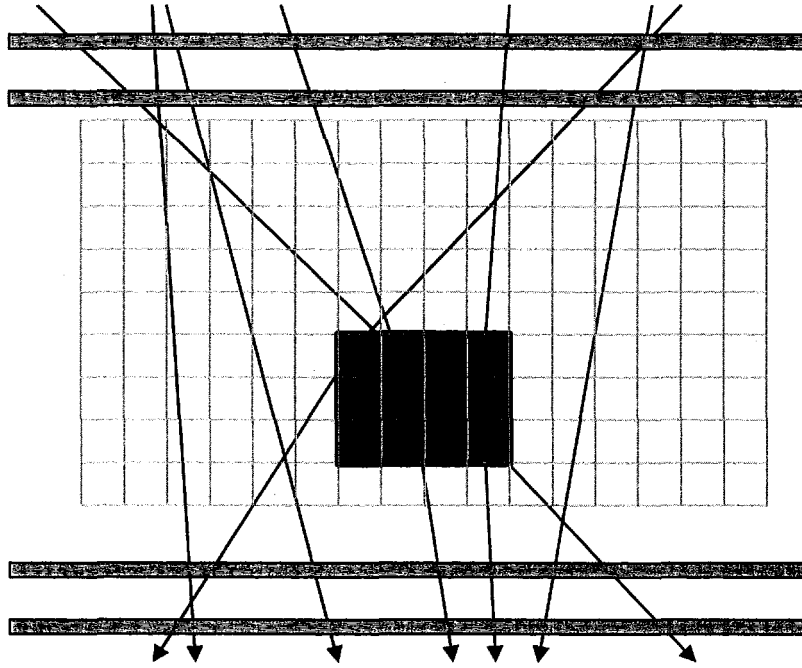


**Figure 11 – Cosmic Ray Muon Radiography.** The basic concept is that individual muons are tracked into and out of an object area via muon detectors (shown in orange). Those rays that pass through a dense object (shown in red) will experience scattering. Those rays that do not pass through the object (shown in black) experience relatively little scattering. The structure of the object can be reconstructed via tomographic methods based on the information from many rays passing through the object volume.

The bend angle of each track is computed. As many rays pass through the object volume from different angles and positions, an aggregate dataset is created. Tomographic reconstruction techniques may then be applied to this dataset to reconstruct the structure of objects within the object volume.

### **3.2 Preliminary Calculations on Exposure Time**

We have described the feasibility of tracking individual muons due to the low event rate. An obvious first question is: “is the event rate high enough to provide information in a reasonable amount of time?”

#### **3.2.1 Material Discrimination Assuming Monoenergetic Muons**

Let us consider three cubes, 10 cm on a side, one formed of concrete, another of iron, and a third of uranium. We’ll assume that cosmic ray muons pass through these cubes at the sea level rate of 100 muons/minute. For simplicity, we will ignore varying path lengths and assume that all rays pass through 10 cm of material. If we count for one minute, we get, on the average, 100 muons through each cube. We measure the tracks of the muons, and compute scattering angles in each of the two orthogonal coordinates. Call these measurements  $\theta_x$  and  $\theta_y$ . We’ll ignore the effect of muon energy spread for the moment and assume that all particles are at the mean energy of 4 Gev.

So for each cube, in one minute, we obtain 200 measurements of scattering angle. From these measurements we calculate, for each cube, the mean square scattering, which is an

estimate of the variance of the underlying Gaussian scattering distribution. We may express 99% confidence intervals on each variance estimate ( $\hat{v}$ ) as [21]:

$$\frac{200\hat{v}}{\chi_{.005}(200)} < \theta_0^2 < \frac{200\hat{v}}{\chi_{.995}(200)} \quad (16)$$

Using Eqs. (1) and (16), we present in Table 4 the confidence intervals expected in one minute of muon tracking. Clearly we are able to distinguish between the three materials in less than one minute.

Table 4. Confidence intervals on scattering after one minute of tracking 4 Gev muons through 10 cm of various materials.

Material	99% Confidence Intervals on RMS Scattering, milliradians	
	LCL	UCL
Concrete	2.9	3.8
Iron	7.6	9.9
Uranium	19.0	24.6

As a check on these numbers, we used Eq. (1) to randomly generate scattering of 4 Gev muons through these materials. We generated 200 scattering measurements at a time, made the  $\hat{v}$  estimates, and then repeated this experiment 1,000 times. Results are shown in Figure 12 with 99% confidence intervals (assuming normal distributions for simplicity) that are close the accurate values of Table 4.

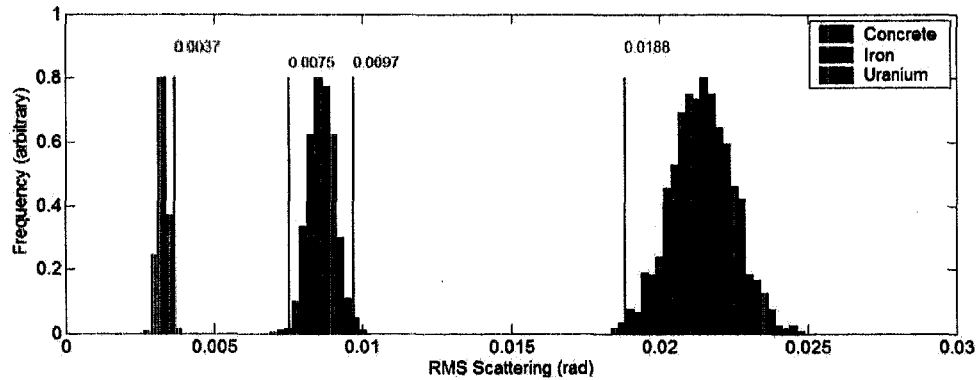


Figure 12 – Discrimination of materials using scattering of 4 Gev muons with ~1 minute of exposure (simulated results). Approximate 99% confidence intervals are shown.

Cosmic ray muons arrive with a range of energies, and this fact will increase the variance of the estimates over those shown in Table 4. Since the energy distribution of cosmic rays muons may only be described through partially empirical models, we cannot assess the effect of energy spread analytically. However, we can estimate the effect via simulation, as described in the following section.

### 3.2.2 Material Discrimination Assuming Cosmic Ray Muon Energy Spread

The arrival angle and energy distribution of cosmic ray muons was discussed in Section 2.1.2. This distribution has been experimentally documented and has been modeled via a



mixture of theoretical and empirical methods. One such model, developed by Gary Blanpied [8] is described in Appendix 1. Code based on this model was used to generate a dataset of 1,000,000 muons conforming approximately to the documented angular and energy spectrum.

Passage of these muons through the concrete, iron, and uranium cubes of the previous section was simulated using Eq. (1). We again took muons, 200 at a time, and made the mean square scattering estimates  $\hat{v}$  as described in the previous section. We performed this experiment 1000 times to assess the variability in the scattering estimates. Results are shown in Figure 13. The distributions are not normal, but approximate 99% confidence intervals, assuming normality, are shown. The three materials are distinguishable from one another in this simulated one minute exposure under the normality assumption, but most of the margin apparent in Figure 12 is gone.

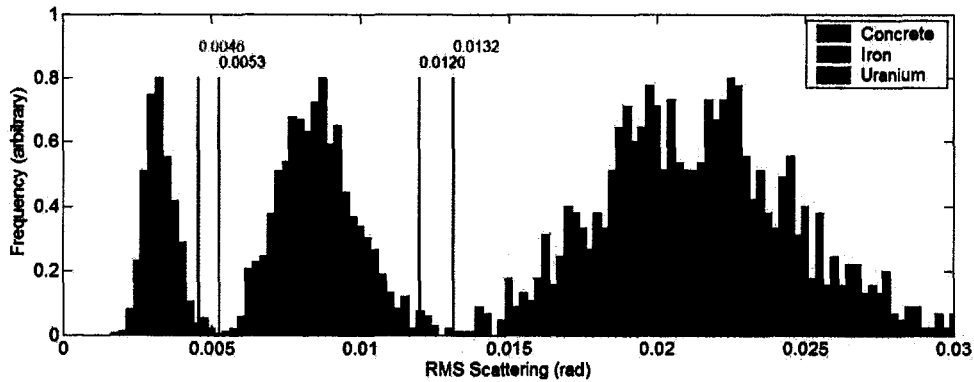


Figure 13 – Discrimination of materials using scattering of muons with energy drawn from a model of the cosmic ray energy spectrum; ~1 minute of exposure (simulated results). Approximate 99% confidence intervals are shown.

Additional factors not considered in this simple analysis (varying path lengths, measurement errors, etc.) will certainly be present in a real implementation and will increase required exposure time. However, these preliminary calculations indicate that material discrimination with minute-order exposure times is probably achievable.

If we could measure particle momentum, we might be able to normalize the scattering signal in some way and recover some of our margin for one minute material discrimination. We discuss this further in Section 3.5.

### 3.3 Point of Closest Approach (PoCA) Reconstruction Method

In this section we will describe a relatively simple, preliminary reconstruction technique that we have developed which takes advantage of multiple scattering. In this preliminary technique we depart substantially from the traditional tomographic methods discussed in Section 2.5 (though we propose to also investigate the application of algebraic methods to this problem).

For simplicity of description, let us consider a two dimensional situation, though our method will be extended to three dimensional reconstruction in a straightforward manner. We first overlay the object area with a uniform grid, as was shown in Figure 11. We will

seek to reconstruct some metric relating to material density, assuming that this metric is constant within each cell in the grid.

Consider a single ray passing through an object area (see Figure 14), with position/angle detectors as previously described. The scattered path of the ray will be stochastic (Figure 14a), as was described in Section 2.2.3. We cannot know this path, of course, but will be able to measure the bend angle of the ray ( $\Delta\theta$ ) by tracking incoming and outgoing ray angles. We may take  $\Delta\theta^2$  to be the “signal” or “path integral” of the ray. If the bend angles are small (perhaps tens of milliradians) with respect to the size of the cells in our grid (perhaps a centimeter or larger on a side), then we may approximate the ray path as the straight line connection between entry and exit points (Figure 14b). One approach would be to spread the signal over all cells through which the ray was estimated to pass, weighted by the path length within each cell. If we assume, however, that the object volume contains small objects, and thus wish to localize the scattering signal, we can take advantage of additional information to apply a different approach. Let us trace the incoming and outgoing tracks inward to the point of intersection (or point of closest approach for a three-dimensional system) and locate the cell containing that point (Figure 14c). Then let us assume that all scattering resulted from material located within that cell. Finally, let us assign to the cell of intersection the signal  $\Delta\theta^2$  and assign 0 to the rest of the cells containing the ray path (Figure 14d). As many rays pass through the object area, we compute, for each individual cell, the average signal contributed by all rays that were influenced by that cell to obtain our final reconstructed cell value.

The idea of tracing incoming and outgoing ray trajectories to determine a point of scattering was suggested by Charpak, et al. [31], wherein the nuclear scattering represented true “point scattering,” whereas in our case the scattering is distributed.

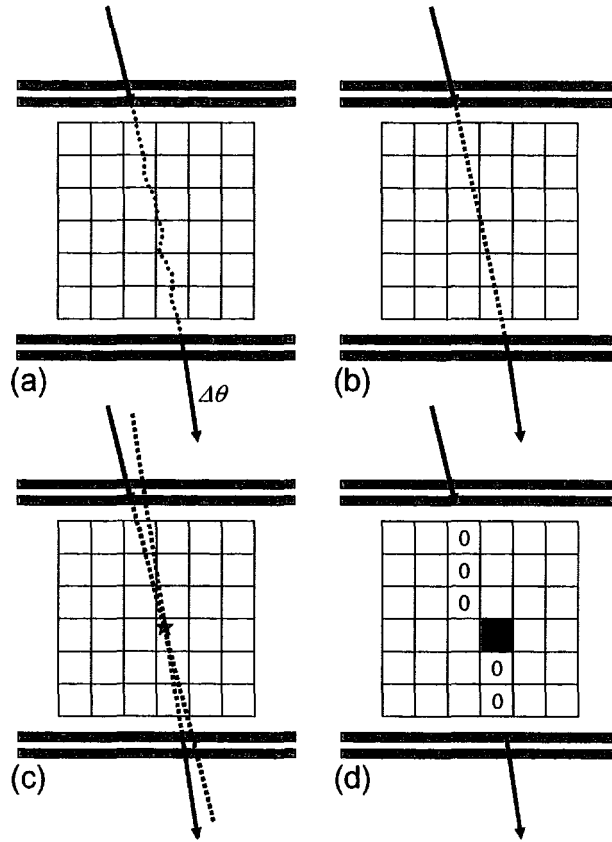
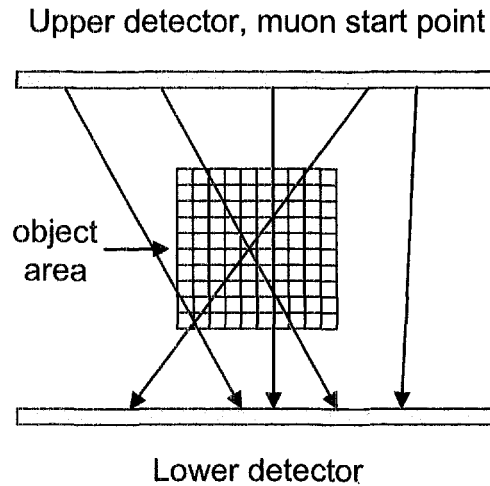


Figure 14 – Illustration of point of closest approach reconstruction. A ray's stochastic path through an object area, with a uniform grid overlaid (a), the estimated ray path created by connecting the entry and exit point of the incoming and outgoing rays (b), finding the intersection point (or point of closest approach in three dimensions) of incoming and outgoing rays (c), and assignment of cell weightings for this particular ray (d). The weights contributed by all rays are averaged to determine the final cell values.

### 3.4 Preliminary Simulated Demonstration

We tested the PoCA reconstruction algorithm through a simple two dimensional simulation. The setup for our simulation is illustrated in Figure 15. Two “detectors,” each 30 cm wide, were implemented, separated by 20 cm vertically. 4 Gev muons were emitted from the upper detector location with random starting position and angle uniformly distributed over  $\pm\pi/4$  radians from vertical. This angular distribution does not accurately reproduce the cosmic ray muon spectrum, but does provide for preferentially vertical orientation. Muon positions and scattered angles were recorded at the bottom detector position. A 10 x 10 cm object area, broken into 1 cm square cells, was centered within the detectors. For these tests, material was placed only in the object area with each 1 cm square cell capable of containing a different material. Muons were tracked through 0.2 cm square elements along their track from upper to lower detectors. For muons entering an element populated with material, scattering was simulated by randomly drawing a scattering angle from a normal distribution with zero mean and standard deviation determined by Eq. (1).



**Figure 15 -- Setup for muon scattering simulation and PoCA reconstruction testing.**

For our first test, we placed a 2 cm square of iron in the center of the object area. Using Eq. (1), with 4 GeV muons and a radiation length of 1.76 cm, we populated centermost four 1 cm square cells in the object area with the value 6.3 milliradians<sup>2</sup>. We then emitted 10,000 muons from the upper detector and performed the PoCA reconstruction. Results are shown in Figure 16. The placement of the iron square is shown in Figure 16a. The PoCA reconstruction is shown in Figure 16b. The iron square is clearly reconstructed with cell values close to that of the original object (the average of the four cell values corresponding to the object is 5.8 milliradians<sup>2</sup>). A slight blur in the vertical dimension may be noted. For comparison a reconstruction wherein ray information was spread along the path of the ray is shown in Figure 16c. Clearly, for this small object, localizing the scattering signal via PoCA was beneficial.

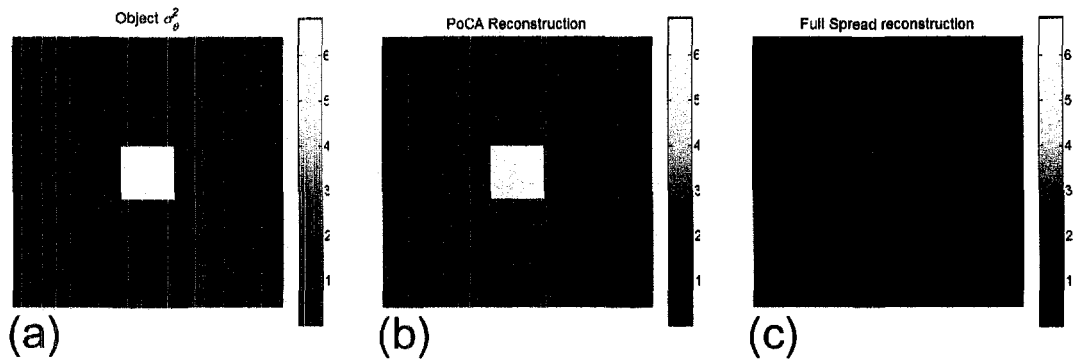


**Figure 16 -- Simplified simulation of muon radiography of an iron block. Illustration of the iron block (a), the PoCA reconstruction (b), and a reconstruction without using localization via PoCA (c).**

To understand the vertical blur in Figure 16b, we may examine the points of closest approach that were used in the reconstruction. Figure 17a shows those points. Although the points are largely within the area of the object, some points are not, which results in blur in the reconstruction. Since rays are predominantly vertical, the blur appears in the vertical dimension. This effect is mitigated by the fact that the PoCA for rays with large bend angles, which contribute to the reconstruction most significantly, lie almost

completely within the object area, as shown in Figure 17b. The vertical blur is quite noticeable in Figure 16c, which illustrates the under sampling of the vertical structure in the scene due to lack of horizontal rays (refer to section 2.5.1).

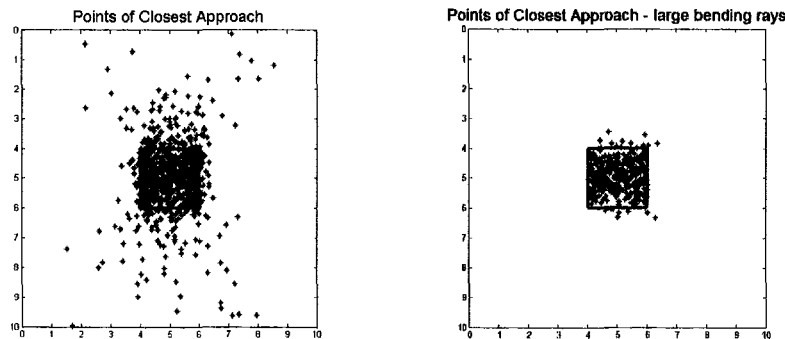


**Figure 17 – Points of Closest Approach for the reconstruction of Figure 15b. PoCA for all rays in shown in (a). In (b), only rays with bend angles greater than the mean square angle for iron are shown.**

For our second test, we placed squares of uranium ( $39.3 \text{ milliradians}^2$ ), iron, and concrete ( $.9 \text{ milliradians}^2$ ) side by side in the object volume, as illustrated in Figure 18a. The PoCA reconstruction is shown in Figure 18b. The positions and relative densities of the objects are well reconstructed (the mean reconstructed cell value for uranium is  $40.4 \text{ milliradians}^2$ , for iron  $5.7 \text{ milliradians}^2$ , and for concrete  $0.8 \text{ milliradians}^2$ ). Some vertical blur is again present. PoCA values are shown in Figure 18c.

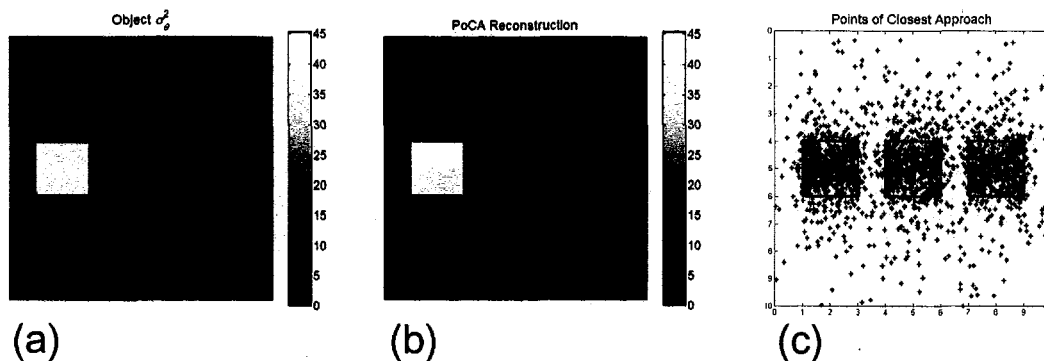


**Figure 18 – A simulation of radiograph of several materials. The objects are formed of uranium, iron, and concrete (a). The PoCA reconstruction (b). Points of closest approach (c).**

These results are encouraging, though there are some deficiencies that must be investigated. We have mentioned the vertical blur due to lack of sufficiently horizontal rays. Another problem is that, for larger objects, this preliminary PoCA algorithm localizes the scattering signal too much, as illustrated in our final example. For this test we used a 4 cm square of iron. Results are shown in Figure 19. Although the shape and dimension of the object is fairly accurately reconstructed, the material has been “lumped” toward the center of the object. The mean cell value in the iron area is  $5.8 \text{ milliradians}^2$ , but the peak value in the center is  $12.3 \text{ milliradians}^2$ .

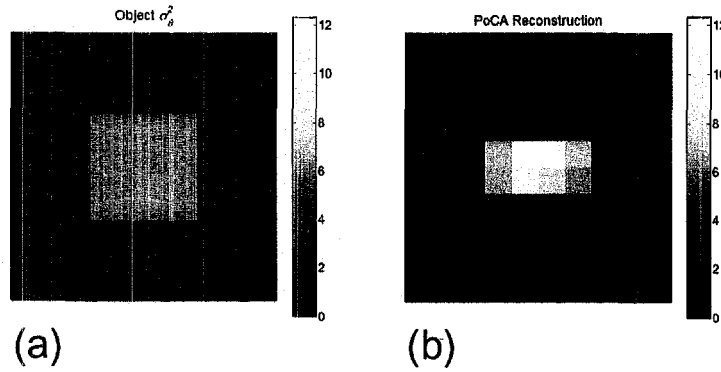


Figure 19 – Simulation of radiography of a larger iron block. The object (a), and the PoCA reconstruction (b).

In summary, these simulations are intended demonstrate the possibility of using multiple scattered cosmic ray muons to approximately reconstruct object density (in terms of multiple scattering tendency, which roughly follows material  $Z$ ). We have shown this possibility through a simple reconstruction method. Refinement of reconstruction methods will be proposed herein.

### 3.5 Momentum Measurement

We showed, in sections 3.2.1, that our ability to discriminate between materials is degraded due to the energy spread of the cosmic ray muons. It is perhaps more appropriate to say that we overstate our ability to discriminate between material when we assume, in analytical calculations or simulations, that the muon source is mono-energetic. In the descriptions and simulations of the previous two sections, we took our scattering signal to be the square of the bend angle of each ray,  $\Delta\theta^2$ . Let's assume that we can make some sort of estimate of the momentum of each ray; call that estimate  $\hat{p}$ . We could then normalize the scattering signal for that ray:

$$\Delta\theta_{adj}^2 = \Delta\theta^2 \left( \frac{\hat{p}}{4 \text{ GeV}} \right)^2 \quad (17)$$

to obtain the scattering signal normalized to the mean energy.

Obtaining a precise measurement of particle momentum is expensive. The most common means [9] is to create a magnetic field through which the charged particles pass. The charged particles will be deflected by the field to a degree inversely proportional to momentum, and by measuring the curvature of the tracks momentum can be inferred. It is possible that such a scheme could be applied for our application, but generating a large area magnetic field would be expensive. Moreover, we probably do not need precision measurements of momentum.

Let's first make a rough assessment of the error involved in making no momentum measurement, but assuming that each particle has the mean momentum. Taking 1,000,000 muons from the Blanpied [8] muon generator, we calculated the uncertainty of assuming that muon energy was at the mean value as follows:

$$\frac{\Delta \hat{p}}{p} := \frac{\sqrt{V(p)}}{E(p)} \cong 200\% \quad (18)$$

In other words, if we assume that all particles have the mean momentum, we will, on the average, be 200% off in our estimate of momentum. This calculation is based on Gaussian statistics, and the cosmic ray spectrum is not a normal distribution, but we will use this estimate for the moment.

We have seen, from the discussion in section 3.2, that our ability to discriminate material in the absence of momentum knowledge is poorer than when we know momentum exactly, but we can still discriminate between uranium, iron, and concrete in modest exposure times. Perhaps we could make a very rough, inexpensive measurement of momentum and improve our results somewhat.

An idea for measuring momentum using multiple scattering is illustrated in Figure 19. We add additional detectors below the object area, along with slabs of material of known thickness and composition. We make a number of scattering measurements (with the setup shown in Figure 20, where two slabs are shown, we can make 4 such measurements) and infer muon momentum. If we use our scattering measurements to create the estimate  $\hat{\sigma}_\theta$ , we can make rearrange Eq. (1) to produce a momentum estimate:

$$\hat{p} = \frac{13.6 \text{ Mev}}{\beta c \hat{\sigma}_\theta} z \sqrt{\frac{L}{L_0}} \left[ 1 + 0.038 \ln \left( \frac{L}{L_0} \right) \right] \quad (19)$$

where  $L/L_0$  is now known. We may then use our momentum estimate to adjust the object scattering signal per Eq. (17).

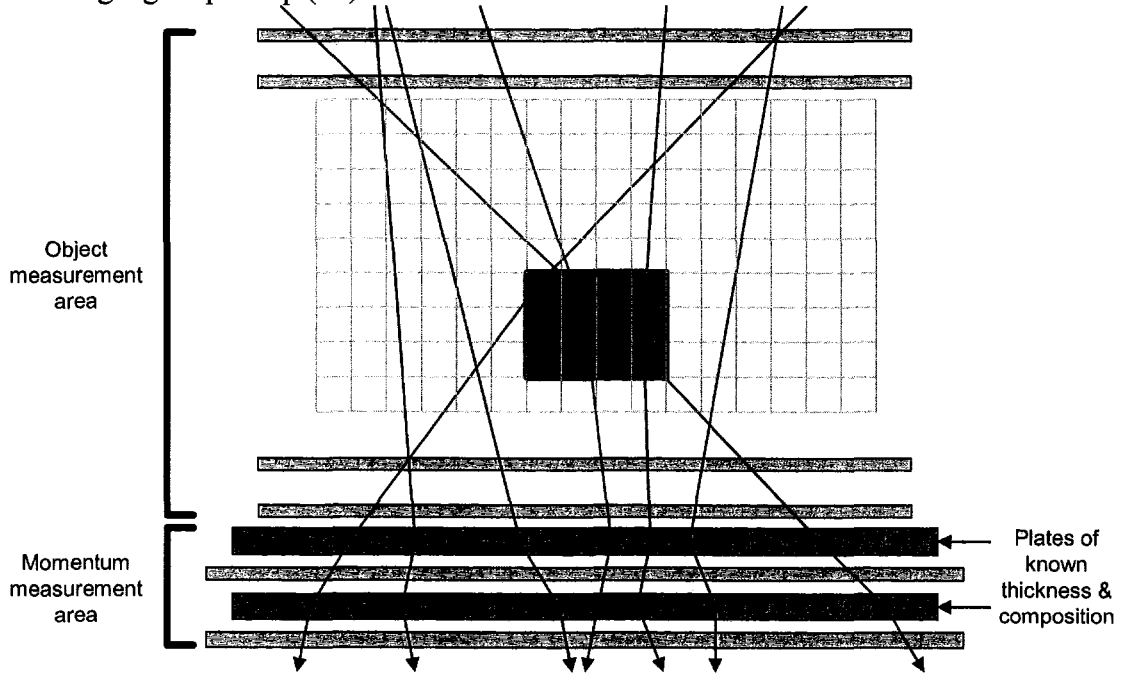


**Figure 20 – Illustration of muon momentum measurement via multiple scattering through layers of material of known thickness and composition.**

We can show that, if we make our momentum estimate from 4 measurements of scattering using the setup shown in Figure 19, we can achieve a mean momentum uncertainty of:

$$\frac{\Delta \hat{p}}{p} \cong 50\% \quad (20)$$

which represents a factor of 4 reduction in our uncertainty when making no measurements.

To check the adequacy of this rough measurement of momentum, we repeated the analysis of sections 3.2.1 and 3.2.2, but added simulation of scattering of each ray through two additional 5 cm plates of iron. Using the four scattering measurement so obtained, we made our estimate of  $\hat{p}$  using Eq. (19), then used Eq. (17) to generate the normalized scattering signal. Using these normalized signals, we repeated the analysis described in Section 3.2 (1000 experiments, each using 200 measurement) with results shown in Figure 21. Use of this rough measurement of momentum substantially improves our one minute material discrimination ability.

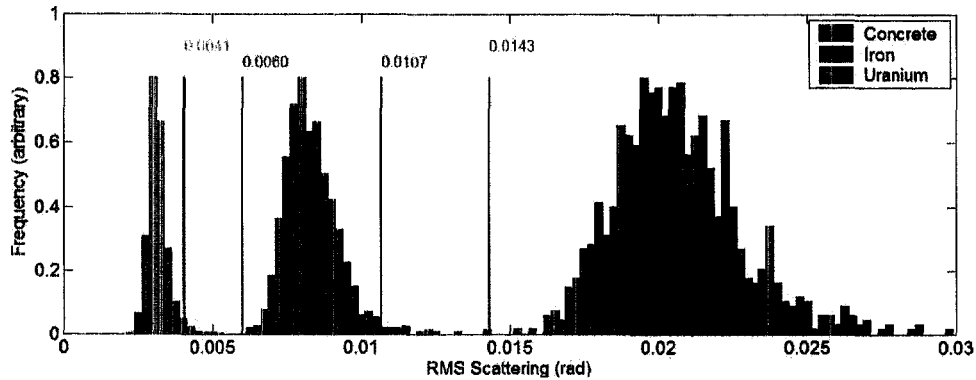


**Figure 21 – Discrimination of materials using scattering of muons with energy drawn from a model of the cosmic ray energy spectrum, but with signal normalized using a rough measurement of momentum; ~1 minute of exposure (simulated results). Approximate 99% confidence intervals are shown.**



## 4. Proposed Work

In this section we describe three main components of our proposed extension to the work presented in Section 3. First, we propose to verify the feasibility of cosmic ray muon radiography experimentally through the construction and testing of a prototype. Because the experimental prototype will be small in scale and without all the capability that we wish to investigate, we also propose to develop and validate a Monte Carlo simulation of the system. Armed with these tools, we propose to investigate reconstruction techniques, seeking to make optimal use of the information provided by scattered muons. Finally, we briefly describe one possible practical application of the technique.

### 4.1 Experimental Prototype

#### 4.1.1 System Overview

Although the physics underlying cosmic ray muon radiography are well understood, and good methods for detecting muons exist, we view an experimental demonstration to be a key component of proof of feasibility. We propose to build a small system from legacy equipment available at the Los Alamos Neutron Science Center (LANSCE). The basic required system components are shown in Figure 22.

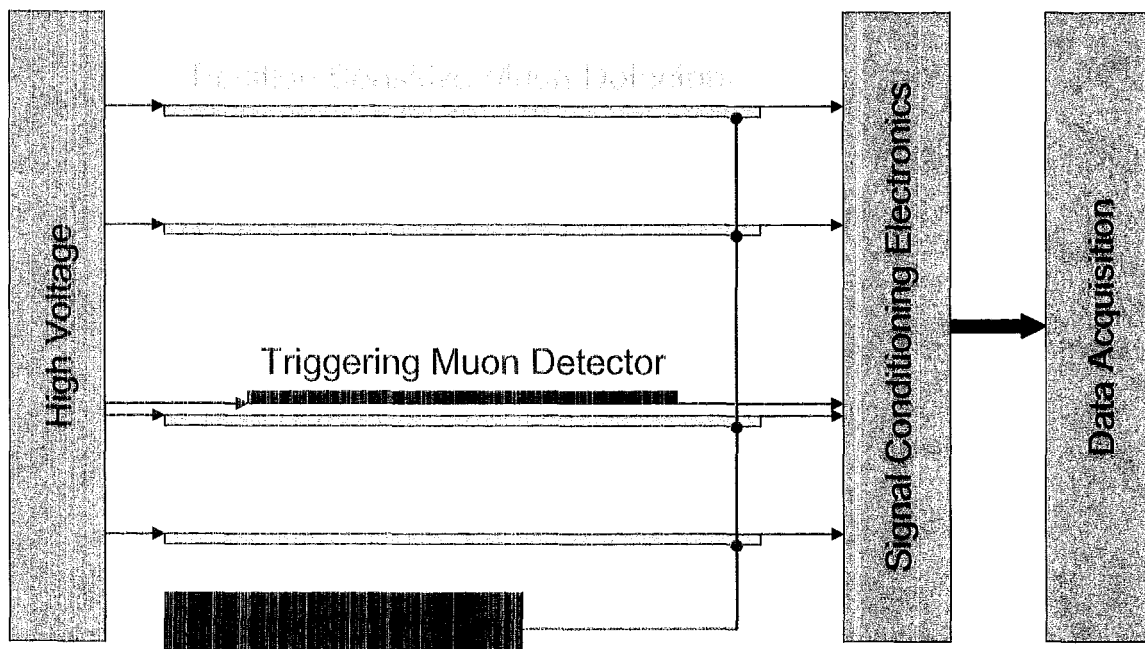


Figure 22 – System components for proposed muon radiography experimental prototype.

Position sensitive muon detectors are available for our use, having been decommissioned from a spectrometer used at LANSCE. Some details on the operation of these detectors will be discussed in the next section. A high voltage ( $\sim 2000\text{V}$ ) power supply will be used to energize these detectors, and a source of ionizable gas will be required. A triggering detector may be required, since the position sensitive detectors rely on time delayed signals to indicate particle position. Signal conditioning electronics (amplifiers, discriminators, digital logic elements, etc.) are also available at LANSCE. Data

acquisition will likely be done using a LANL developed PC-based system [22], a previous version of which was used to capture data in the spectrometer application.

We must stress that our objective in building such a system to demonstrate the feasibility of cosmic ray muon radiography as quickly and inexpensively as possible. We do not seek to construct a state of the art instrument, but plan to use, where possible, legacy equipment on hand that will do the job.

#### 4.1.2 Time Delay Line Multi-Wire Proportional Chamber (MWPC) Detectors

Wire chambers were pioneered by Charpak [23] in the late 1960's, and continue to be used in many applications today [24]. A cross section through a generic wire chamber is shown in Figure 23. Anode wires are stretched between two cathode plates and a voltage of a few kV is applied. The resultant field lines are shown. When an ionizing particle passes through the chamber ion pairs are created. The electrons produced drift toward the anode wires. As the electrons get very near the wires and the field strength increases, they are accelerated with sufficient energy to create additional ion pairs and an avalanche results (particularly when the chamber is filled with a counter gas designed to promote ionization). The avalanche of electrons produces a negative pulse on the anode wire. In some wire chambers each anode wire is connected to an amplifier and pulse shaper. In its most primitive form such a chamber can measure particle position to the spacing of the anode wires. By adding a fast triggering, but non position sensitive detector such as a scintillator and measuring the time between the scintillator signal and the wire chamber pulse, the distance between the particle and the wire can be inferred, improving position resolution. The careful reader might note that when a particle produces a signal on a wire, it is ambiguous which side of the wire the particle was on. This problem can be overcome by interspersing cathode wires between each anode wire and detecting the induced positive pulses on cathode wires to resolve the side to side ambiguity [25]. One may also simply stack two chambers atop each other, with anode wire positions offset by half the anode wire spacing. To measure particle position in two orthogonal coordinates a stack of chambers may be constructed with wire directions oriented in those orthogonal directions.

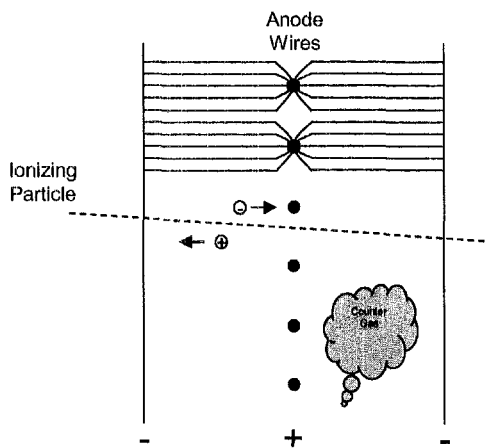
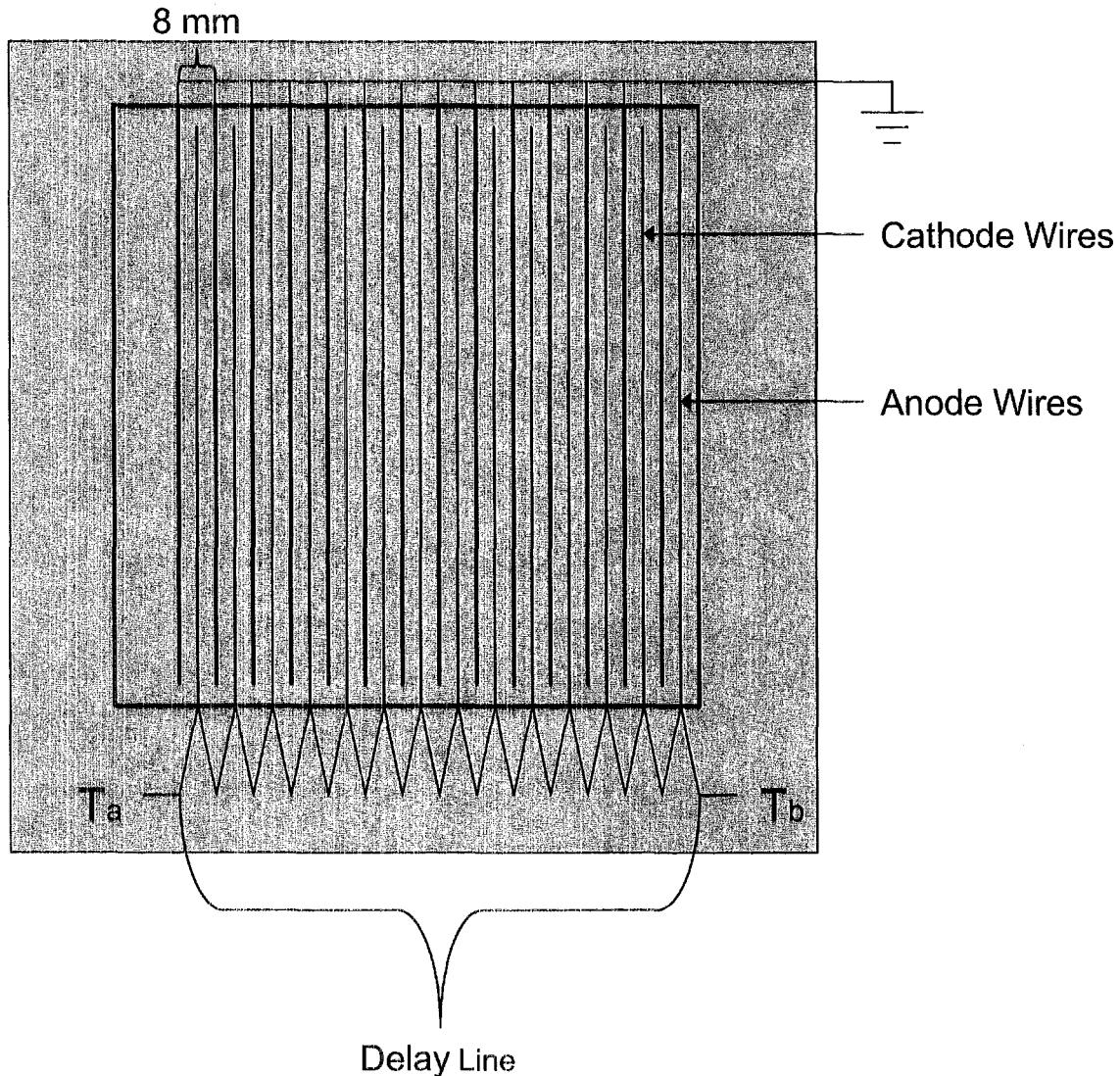


Figure 23 – Cross-section of a generic multi-wire proportional chamber (from [24], used with permission).

We propose to use (due to their availability) a form of MWPC that incorporates time delay lines (TDL) to read out anode pulses, reducing the amount of electronics required. As illustrated in Figure 24, the anode wires are all connected to a delay line which produces a signal delay of  $2.5 \text{ ns}\cdot\text{cm}^{-1}$ . When a pulse occurs on a particular anode wire, the pulse appears at differing times at two readout nodes. The difference between these times may be used to identify the particular anode wire, and the sum of the times may be used to measure drift time and infer distance from the wires. We propose to use multiple wire chambers with offset wire locations to resolve wire side ambiguity. A position resolution of 0.35 mm (FWHM) has been reported for these devices [26].



**Figure 24 – Schematic of time delay line MWPC.**

So each position sensitive detector shown in Figure 22 will actually be comprised of four TDL MWPC's, two pairs with wire orientations in orthogonal directions. If we achieve 0.40 mm (FWHM) position resolution, and space the chambers vertically at 20 cm, we

should achieve 2 milliradian (FWHM) angular resolution, which should be sufficient for our purposes.

It is worth noting that Frlez, et. al. [14] in their previously mentioned use of cosmic rays for efficiency testing of cesium iodide crystals, successfully used TDL MWPC's identical to those proposed herein and in a configuration very similar to our proposal. We have high confidence that this detection system will work.

#### **4.1.3 Signal Conditioning Electronics, Data Acquisition, and Analysis.**

For each wire chamber, we expect to need two amplifiers and two discriminators (analog pulse to digital pulse converters). Using a trigger pulse from the scintillator, we will feed the digital wire chamber signals into a time to digital converter system and capture this data using a PC-based data acquisition system. Our dataset will then consist of pulse times from all the wire chambers for each event. We will need to develop and apply analysis software to convert these times into particle positions at each chamber location. All of these steps were required in the spectroscopy application wherein the TDL MWPC's were previously used, so we are confident that we can update the previous electronics, data acquisition, and analysis software for our prototype.

#### **4.1.4 Demonstration**

After construction and calibration of the prototype, we will select test objects to demonstrate feasibility of the technique. We will also verify results against theoretical expectations.

### **4.2 Simulation and Validation**

We will develop a Monte Carlo simulation of the system. Several packages which simulate the required physics are available ([27], for example), or we may develop our own Monte Carlo code. In either case, we will validate the simulation against results obtained from the prototype system. Since the prototype system will be small scale, with narrow acceptance angle for cosmic rays, we expect to need such Monte Carlo code to investigate larger scale applications of the technique.

### **4.3 Reconstruction Algorithm**

We described and demonstrated our new PoCA reconstruction technique in Sections 3.3 and 3.4. We propose to investigate the following additional threads related to reconstruction:

1. Traditional algebraic tomographic reconstruction. We will investigate the use of traditional algebraic reconstruction techniques (see Section 2.5.2), using scattering as the information source (ignoring ray displacement and the geometric information used in PoCA). We expect to find that reasonable reconstructions can be made but will suffer from the lack of horizontal illumination. However, we can envision applications wherein an object could be rotated within the instrument to overcome this deficiency.
2. Refinement of PoCA. An advantage of PoCA over simple tomographic methods is that we can localize the scattering signal along the ray path, overcoming, to a

certain extent, our lack of “horizontal projections.” We highlighted some of the deficiencies of the PoCA algorithm in our demonstration in Section 3.4 and will be considering application of additional information to improve performance. For example, the distance at point of closest approach should provide information of the degree to which the scattering signal should be distributed along the ray path. If the ray encounters a very small object (in the limit, consider a “point scatterer”) then the incoming and outgoing rays will very nearly cross. If a ray encounters a distributed scatterer, and many multiple scatterings occur, then the distance between rays at point of closest approach will be much larger.

3. Combination of PoCA and tomographic methods. We speculate that the scattering and displacement signals from rays might be combined into an aggregate signal that could be used within a tomographic algorithm, combining the advantages of tomographic and PoCA methods. We propose to first investigate a maximum likelihood formulation of the reconstruction problem.
4. Application of Regularization Methods. Regularization, i.e., the application of mathematical constraints and prior knowledge in the reconstruction process, will be investigated. Some recent work in the use of total variation regularization [28] may be pertinent.
5. Fuzzy Tomographic Methods. This thread is somewhat peripheral to cosmic ray muon radiography itself, but is spawned from the author’s previous research into fuzzy systems [29]. The idea of using fuzzy membership functions instead of square pixels or cubic voxels occurred to us as a means for simplification of the implementation of tomographic reconstruction. It turns out that fuzzy tomography has been demonstrated [30] previously. We speculate that there might be advantages in allowing the reconstruction space to adapt to fit the object, and will pursue this thread as time allows.

The end result of these proposed investigations is to define and demonstrate the most effective reconstruction technique (from among these candidates and any others developed along the way) for cosmic ray muon radiography. We expect to make this determination of effectiveness primarily based on the degree of consistency between the reconstruction and object radiographed. We will also consider practical performance factors such as convergence time.

#### ***4.4 Application to Contraband Detection for Homeland Defense***

The work proposed herein has been funded at Los Alamos National Laboratory. This funding was to investigate cosmic ray muon radiography for the detection of high density contraband in vehicles or shipping containers. Clearly the technique may work well in this application, since it will be sensitive to high-Z materials such as shielded nuclear contraband (see Figure 25).

It is outside the scope of this proposal to fully develop cosmic ray muon radiography for this application. In other words, we expect to have to deal with very application specific issues such as detection thresholds, alpha/beta risk, and practical logistic issues associated with inspection times for example. We do not propose to address such issues

in this proposed work. However, we will likely use the contraband detection problem as a platform to illustrate some of the techniques that we develop.

## 4.5 Summary

In summary, the work proposed herein will be directed towards two primary goals:

- Demonstrate the feasibility of making radiographs using cosmic ray muons. If successful, this will be the world's first such demonstration, and will represent an achievement of some significance.
- Develop appropriate tomographic methods for object reconstruction. New methods, likely based on statistical signal processing, will be required due to the nature of multiple scattering as an information source.

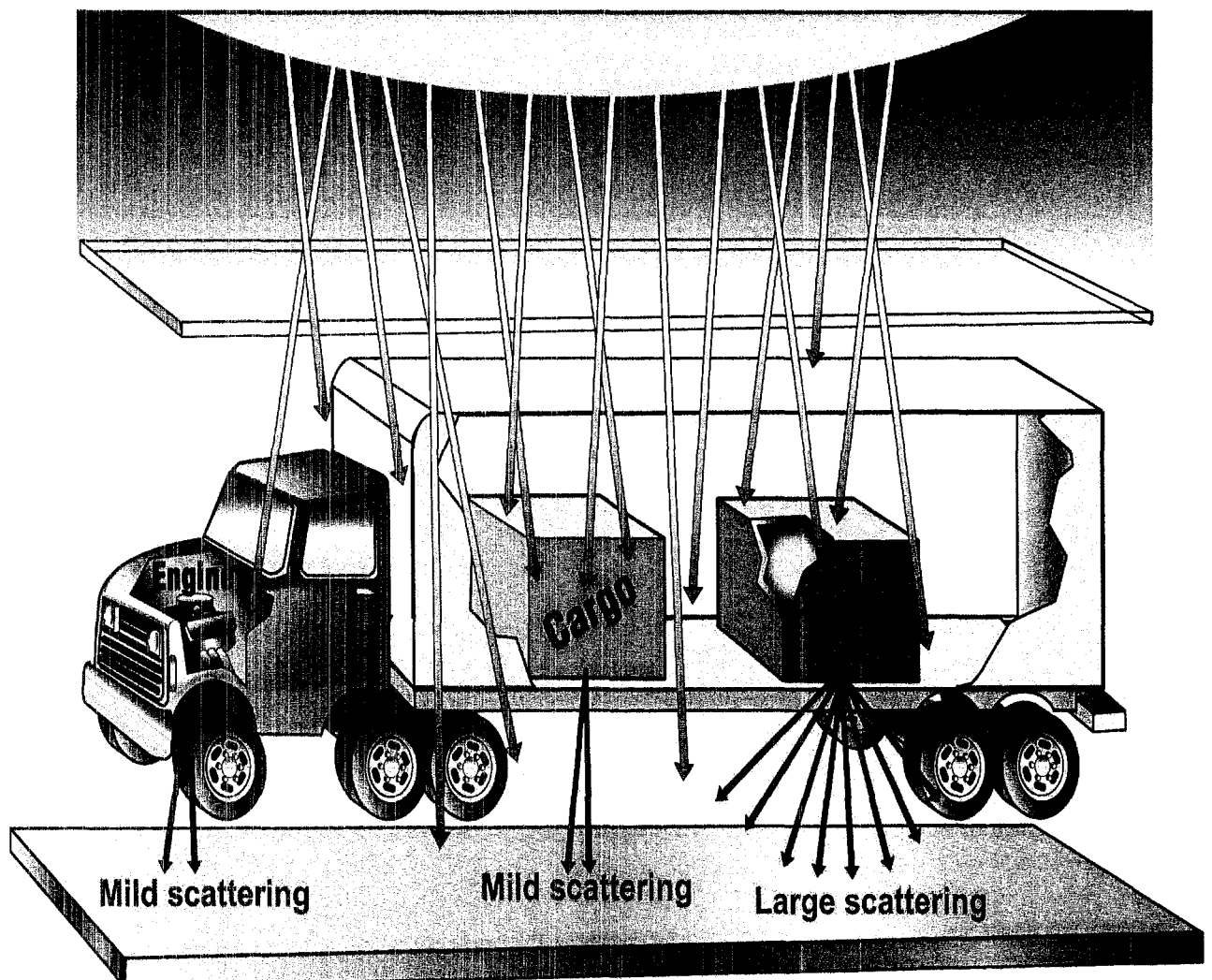


Figure 25 – Illustration of Cosmic Ray Muon Radiography for the detection of contraband in a vehicle.

## **5. Administrative Issues**

### **5.1 Significance**

Cosmic ray muon radiography is a novel concept. Never before has a radiograph of an object been made from cosmic ray muon scattering. No radiograph of objects smaller than pyramids and mountains has been made by any means using cosmic ray muons. The potential to radiograph objects using no artificial dose of radiation and no artificial source (only passive detectors) is quite attractive.

This method may be particularly attractive for the inspection of vehicles at border crossings without irradiation of vehicle drivers or contents. It will be a challenge to extract enough information to make security decisions with exposure times short enough to avoid extending border wait times. Though full investigation of this application is outside the scope of this proposal, the proposed work will feed into that effort, which is undeniably significant.

### **5.2 Appropriateness**

Cosmic ray muon radiography is based on particle physics, and it may be natural to ask: “Is this work electrical engineering or physics?” The physics involved in this proposal is well understood, and we do not propose to make any significant advances in this field. The achievements involved in successful completion of the proposed work are demonstration of a new mode of radiography and development of new computerized tomographic methods to support it. Radiography, tomography, and statistical signal processing are topics of research in many electrical engineering departments..

### **5.2 Timeline**

The work proposed in Section 4 is currently underway, and we believe that it can be completed during the third quarter of 2003. If this proposal is accepted, we expect to establish a target of fourth quarter 2003 for a dissertation defense.

### **5.3 Publication Targets**

If we are successful, we will attempt to publish a description of this concept in a high profile scientific journal such as *Nature* or *Science*. A detailed paper on experimental methods and results will likely be targeted for publication in *Nuclear Instruments and Methods* or *IEEE Transactions on Nuclear Science*. Papers on reconstruction methods, depending on their content may be targeted for publication in *IEEE Transactions on Image Processing*, *IEEE Transactions on Fuzzy Systems*, *IEEE Transactions on Signal Processing*, or the like.

## Appendices

### ***Appendix 1 – Blanpied Muon Generator***

A muon generator used for simulations performed in this proposal was developed by Gary Blanpied of the University of South Carolina Department of Physics and Astronomy, with assistance from Larry Schultz (the author of this proposal). The Blanpied generator provides muons of energies from slightly less than 1 Mev to somewhat greater than 1000 Gev.

The generator is based on a model of pion→muon decay at an altitude of 15km and survival rate of muons passing through the atmosphere to sea level. It was validated against experimental data.

At the root of the model is the generation of a lookup table version of the differential spectrum  $D(E, \theta)$  in  $[\text{cm}^{-2}\text{sr}^{-1}\text{sec}^{-1}\text{Gev}^{-1}]$ . Among many sources, two experimental datasets exist within the literature tabulating  $D(E, \theta = 0^\circ)$  [5] and  $D(E, \theta = 75^\circ)$  [4]. Figure A.1.1 shows the differential spectra from the Blanpied model against experimental data. The fit is pretty good, although the under prediction at low energies is a bit disturbing, since it is from this part of the distribution that we draw most of our useful events. We will investigate this issue during the proposed work.

An often quoted “rule of thumb” is that the spectra with respect to zenith angle is roughly proportional to  $\cos^2(\theta)$  for energies near the mean (about 4 Gev). Plotted in Figure A.1.2 is the model generated differential spectrum against zenith angle for 4 Gev energy muons. Also shown is an appropriately weighted  $\cos^2(\theta)$  curve, showing approximate agreement.



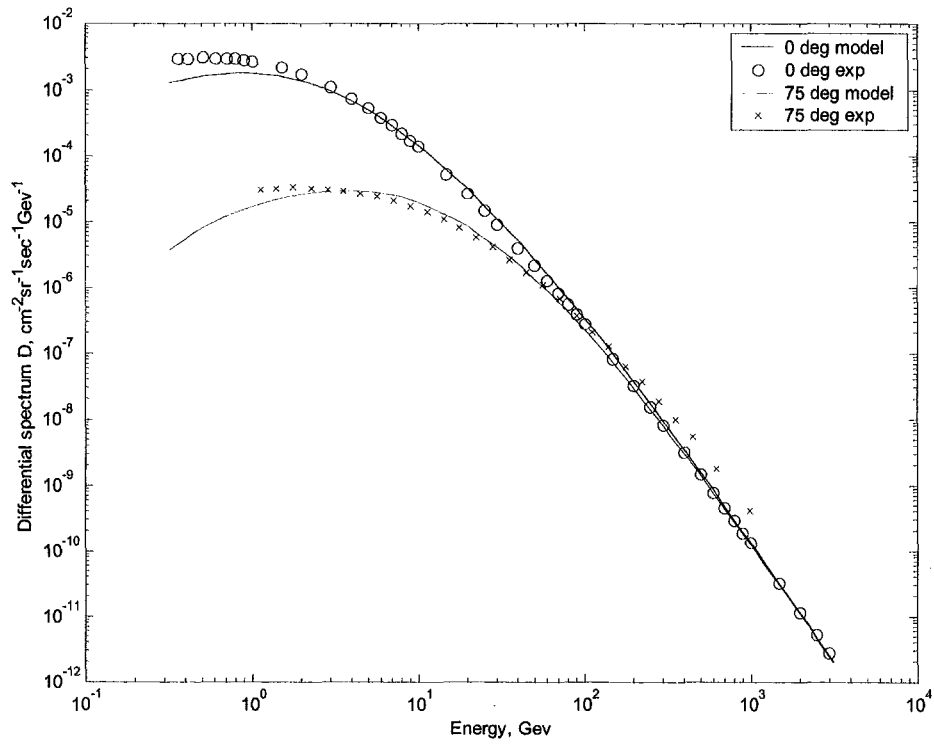


Figure A.1.1 – Comparison of differential muon spectra from model with experimental data.

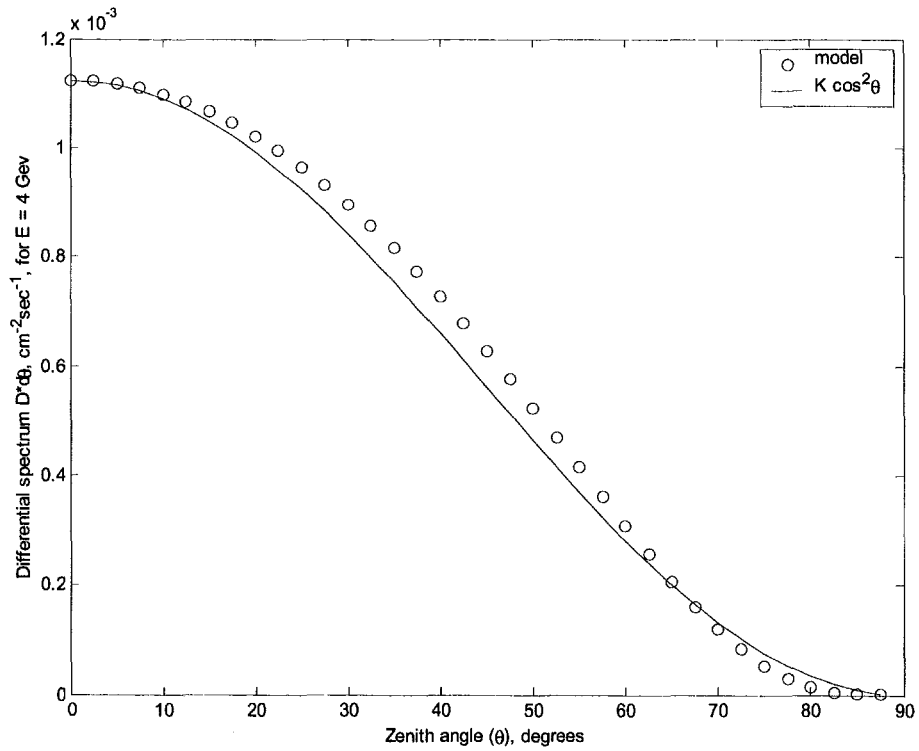
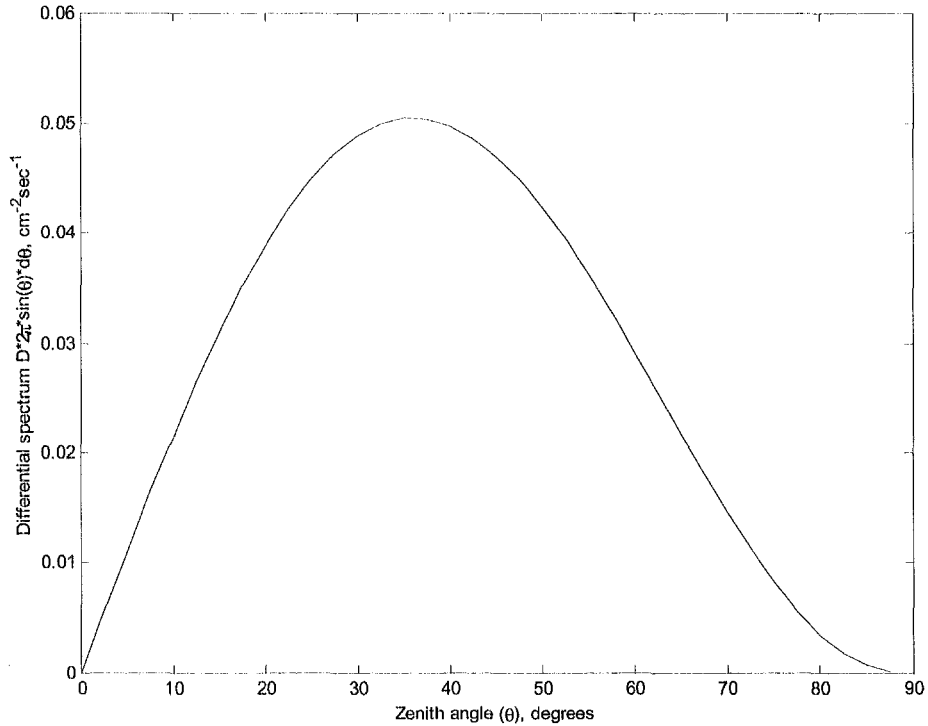


Figure A.1.2 – Model differential muon spectrum wrt zenith angle for  $E = 4$  GeV

However, Figure A.1.2 does not represent the true spectrum for zenith angle in a spherical coordinate system due to solid angle effect. The zenith angle spectrum from the model, adjusted for solid angle, is shown in Figure 3. Because of the solid angle effect, the mean zenith angle is about  $35^\circ$ , with no muons arriving at a  $0^\circ$  angle.



**Figure A.1.3 – Model differential muon spectrum wrt zenith angle, adjusted for solid angle.**

To deal with the coupled distribution in generating muons, the model first selects a zenith angle  $\theta$ , and then selects an energy  $E$  based on the selected  $\theta$ . To do this, the differential spectrum is integrated across the total  $E$  range, and is then multiplied by  $2\pi \sin(\theta)$  to incorporate the effect of solid angle. This result is converted to a normalized table wherein a random number  $[0,1]$  is used to select a  $\theta$ . To select  $E$ , the differential spectrum is integrated and normalized within each  $\theta$  bin to produce an  $E$  selection table for each  $\theta$  bin. After selecting  $\theta$ , the appropriate  $E$  table is used to select  $E$ .

Previous plots have shown the differential spectrum from which muons are drawn. A dataset of 1 million muons was produced from the model. A distribution of energy of those muons is shown in Figure A.1.4. The distribution does not look like the one shown in Figure A.1.1, but does after adjusting for bin size, as shown in Figure A.1.5.

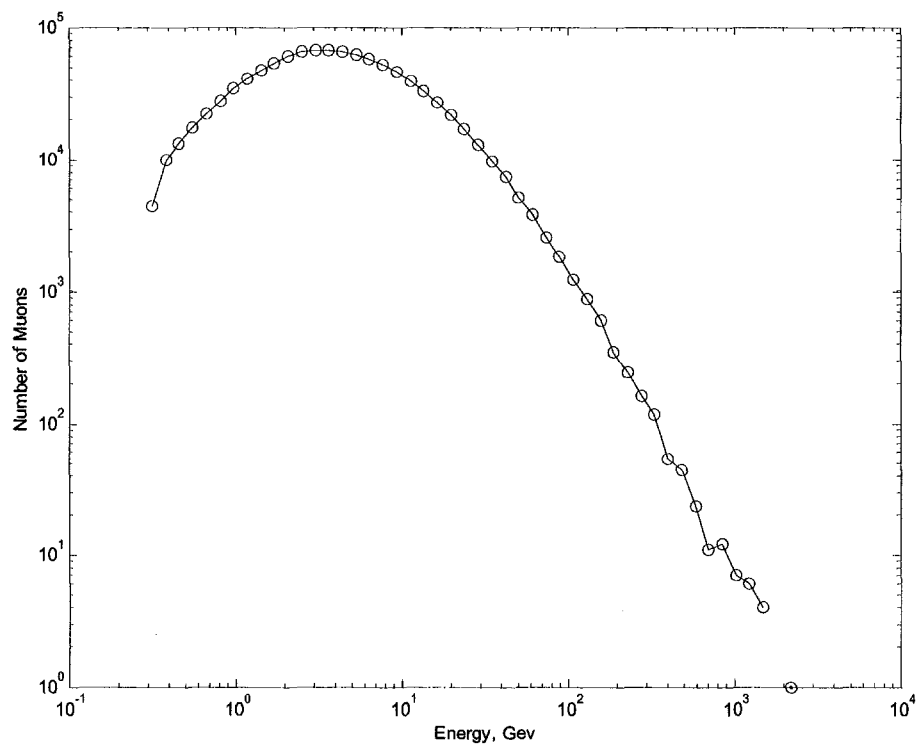


**Figure A.1.4 – Energy distribution of 1,000,000 muons drawn from generator.**

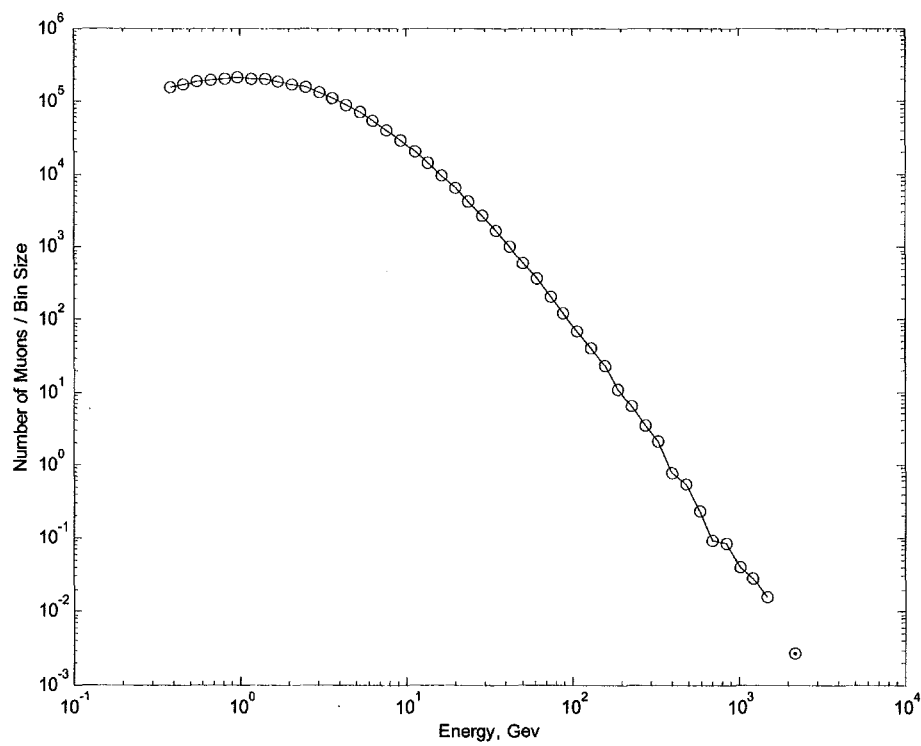


**Figure A.1.5 – Energy distribution of 1,000,000 muons, adjusted for bin size.**

Finally, a histogram of zenith angles of the 1 million muons is shown in Figure A.1.6. This distribution matches that shown in Figure A.1.3, as expected.

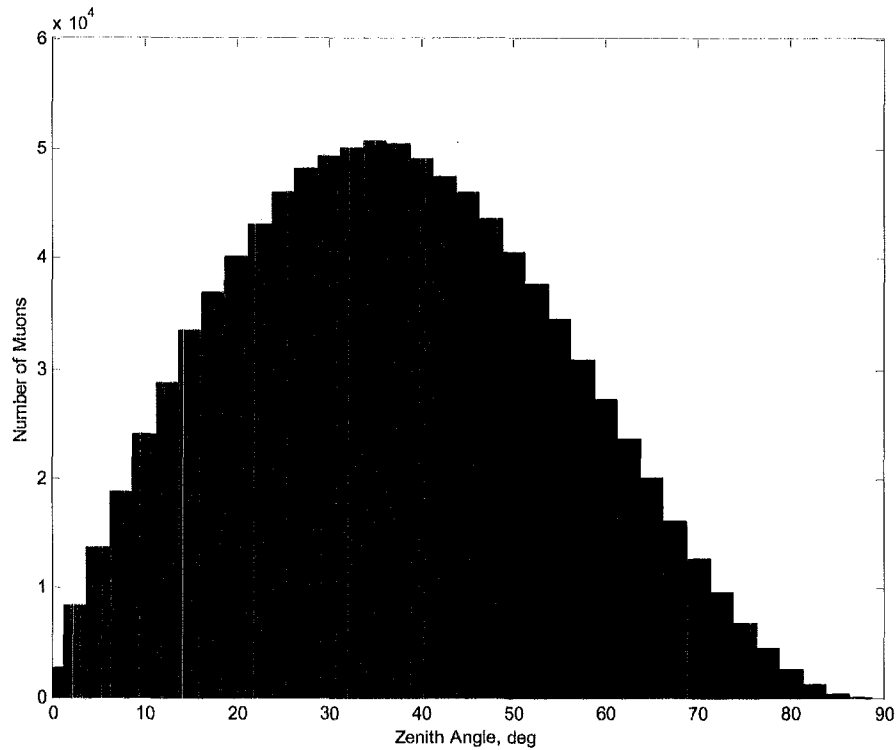


**Figure A.1.6 – Distribution of zenith angles of 1,000,000 muons drawn from generator.**

In summary, the results from muons drawn from the Blanpied generator are congruent with the underlying differential spectra model. That model matches experimental data fairly well, with modest under prediction of the rate of low energy ( $<1$  GeV) muons. We will investigate that discrepancy further, but judged this model to be suitable for preliminary simulations.

## References

- [1] Hagiwara, K., et al., Particle Data Group, Review of Particle Physics, *Physical Review D* **66**(1) (2002).
- [2] Allkofer, O.C., and P.K.F. Grieder, "Cosmic Rays on Earth," *Fach-informationszentrum Energie, Physik, Mathematik*, **Nr 25-1** (1984).
- [3] Dar, A. "Atmospheric Neutrinos, Astrophysical Neutrons, and Proton-Decay Experiments," *Physical Review Letters* **51**(3), pp 227-230 (1983).
- [4] Jokisch, H., et al., "Cosmic-ray Muon Spectrum up to 1 TeV at 75° Zenith Angle," *Physical Review D* **19**(5), pp 1368-1372 (1979).
- [5] Rastin, B., "An Accurate Measurement of the Sea-Level Muon Spectrum within the Range 4 to 3000 GeV/c," *J. Phys. G: Nucl. Phys* **10**, pp 1609-1628 (1984).
- [6] Motiki, M., et al., "Precise Measurement of Atmospheric Muon Fluxes at Sea Level," in *Proceedings of the ICRC 2001*, 927, Hamburg, Germany (2001).
- [7] Sanuki, T., et al., "Atmospheric Muons at Various Altitudes," in *Proceedings of the ICRC 2001*, 950, Hamburg, Germany (2001).
- [8] Blanpied, G., University of South Carolina, Department of Physics and Astronomy, personal communication, June, 2002.
- [9] Rossi, B., *High Energy Particles*, Prentice-Hall, Inc., Englewood Cliffs, NJ (1952).
- [10] Schneider, U., and E. Pedroni, "Multiple Coulomb Scattering and Spatial Resolution in Proton Radiography," *Med. Phys.* **21**(11), pp 1657-1663 (1994).
- [11] Alvarez, L.W., et al., "Search for Hidden Chambers in the Pyramids," *Science* **167**, pp 832-839 (1970).
- [12] Minato, S., "Feasibility of Cosmic-Ray Radiography: A Case Study of a Temple Gate as a Testpiece," *Materials Evaluation* **46**, pp 1468-1470 (1988).
- [13] Nagamine, K., "Geo-tomographic Observation of Inner-structure of Volcano with Cosmic-ray Muons," *Journal of Geography* **104**(7), pp 998-1007 (1995).
- [14] Frlez, E., et al., "Cosmic Muon Tomography of Pure Cesium Iodide Calorimeter Crystals," *Nuclear Instruments and Methods in Physics Research A* **440**, pp 57-85 (2000).
- [15] King, N.S.P, et al., "An 800-MeV Proton Radiography Facility for Dynamic Experiments," *Nuclear Instruments and Methods in Physics Research A* **424**, pp 84-91 (1999).
- [16] Kak, A.C., and M. Slaney, *Principles of Computerized Tomographic Imaging*, SIAM, Philadelphia, PA (2001).
- [17] Hounsfield, G.N., "A Method of and apparatus for examination of a body by radiation such as x-ray or gamma radiation", *British Patent Number 1283915* (1972).
- [18] Gordon, R., "A Tutorial on ART," *IEEE Transactions on Nuclear Science*, **NS-21**, pp 78-93 (1974).

- [19] Widrow, B., and S. D. Stearns, *Adaptive Signal Processing*, Prentice-Hall, Inc., Upper Saddle River, N.J. (1985).
- [20] Haykin, S., *Adaptive Filter Theory*, Prentice-Hall, Inc., Upper Saddle River, NJ (1996).
- [21] Papoulis, A., *Probability, Random Variables, and Stochastic Processes*, McGraw-Hill, Boston, MA (1991).
- [22] Hogan, G. E., "PC DAQ : A Personal Computer Based Data Acquisition System," Los Alamos National Laboratory LA-UR-98-4531 (1998).
- [23] Charpak, G., D. Rahm, and H. Steiner, "Some Developments in the Operation of Multiwire Proportional Chambers," *Nuclear Instruments and Methods* **80**, pp 13-34 (1970).
- [24] Frauenfelder, H., and E. M. Henley, *Subatomic Physics*, Prentice-Hall, Inc., Upper Saddle River, N.J. (1991).
- [25] Breskin, A., G. Charpak, and F. Sauli, "A Solution to the Right-Left Ambiguity in Drift Chambers," *Nuclear Instruments and Methods* **151**, pp 473-476 (1978).
- [26] Morris, C. L., H. A. Thiessen, and G. W. Hoffman, "Position-Sensitive Gas Proportional Chambers," *IEEE Transactions on Nuclear Science*, **NS-25**(1), pp 141-143 (1978).
- [27] GEANT4, <http://geant4.web.cern.ch/geant4/>
- [28] Strong, D. M., and T. F. Chan, "Spatially and Scale Adaptive Total Variation Based Regularization and Anisotropic Diffusion in Image Processing," UCLA Computational and Applied Mathematics Report CAM 96-46 (1996).
- [29] Schultz, L. J., T.T. Shannon, G.G. Lendaris, "Using DHP Adaptive Critic Methods to Tune a Fuzzy Automobile Steering Controller", in *Proceedings of IFSA/NAFIPS 2001*, Vancouver, BC (2001)
- [30] Ichihashi, H., T. Miyoshi, and K. Nagasaka, "Computed Tomography by Neuro-Fuzzy Inversion," in *Proceedings of the 1993 International Joint Conference on Neural Networks*, Nagoya, Japan (1993).
- [31] Charpak, G., et al., "Applications of 3-D Nuclear Scattering Radiography in Technology and Medicine," *Proceedings of the Society of Photo-optical Instrumentation Engineers* **312**, pp 156-163 (1983).